Project Acronym:

MRBREASTBIO (CONCEPT/0521/0040)

MRI breast robotic system for biopsy

Deliverable number: 2.1

Title: Publication in a scientific journal

Prepared by:

Anastasia Antoniou (CUT)
Christakis Damianou (CUT)

Date: 08/05/2023

Co-funded by the European Union

Republic of Cyprus

RESEARCH & INNOVATION FOUNDATION

Table of Contents

Executive summary

This deliverable presents the Journal papers prepared as part of the MRBREASTBTIO project. A manuscript entitled “Phantom-based assessment of motion and needle targeting accuracy of robotic devices for MRI-guided needle biopsy” was submitted to the *International Journal of Medical Robotics and Computer Assisted Surgery* in November 2022. The manuscript was subject to peer review and revision twice, and was eventually accepted and published online in May 2023. It should be noted that an MRI compatible positioning device developed previously by our group was equipped with a biopsy needle and utilized for the purposes of the specific study in order to avoid disclosure of the MRBREASTBIO system.

Another paper entitled “Development and evaluation of a robotic device for MRI-guided needle breast biopsy” **was prepared by the team and will be submitted after the relevant patent application is filed since it includes confidential data** (i.e., detailed description of the system’s components and features), which should not be disclosed prior to the patent application. Otherwise, the technological novelty will be decreased, thus compromising the possibility of obtaining a patent.

Both the published and draft manuscirpts are presented below.

Scientific paper No.1

Received: 16 November 2022 | Revised: 18 April 2023 | Accepted: 24 April 2023

DOI: 10.1002/rcs.2526

ORIGINAL ARTICLE

The International Journal of Medical Robotics and Computer Assisted Surgery WILEY

Phantom-based assessment of motion and needle targeting accuracy of robotic devices for magnetic resonance imaging-guided needle biopsy

Anastasia Antoniou[1] | Anastasia Nikolaou[1] | Nikolas Evripidou[1] | Andreas Georgiou[1] | Antria Filippou[1] | Vasiliki Zinonos[1] | Marinos Giannakou[2] | Antreas Chrysanthou[3] | Cleanthis Ioannides[3] | Christakis Damianou[1]

[1]Department of Electrical Engineering, Computer Engineering, and Informatics, Cyprus University of Technology, Limassol, Cyprus

[2]R&D, Medsonic Ltd, Limassol, Cyprus

[3]Department of Interventional Radiology, German Oncology Center, Limassol, Cyprus

Correspondence
Christakis Damianou, Department of Electrical Engineering, Computer Engineering, and Informatics, Cyprus University of Technology, 30 Archbishop Kyprianou Street, Limassol 3036, Cyprus.
Email: christakis.damianou@cut.ac.cy

Funding information
Research and Innovation Foundation; FUSROBOT, Grant/Award Number: ENTERPRISES/0618/0016; SOUNDPET, Grant/Award Number: INTEGRATED/0918/0008; MRBREASTBIO, Grant/Award Number: CONCEPT/0521/0040

Abstract

Background: The current study proposes simple methods for assessing the performance of robotic devices intended for Magnetic Resonance Imaging (MRI)-guided needle biopsy.

Methods: In-house made agar-based breast phantoms containing biopsy targets served as the main tool in the evaluation process of an MRI compatible positioning device comprising a needle navigator. The motion accuracy of mechanical stages was assessed by calliper measurements. Laboratory evaluation of needle targeting included a repeatability phantom test and a laser-based method. The accuracy and repeatability of needle targeting was also assessed by MRI.

Results: The maximum error of linear motion for steps up to 10 mm was 0.1 mm. Needle navigation relative to the phantom and alignment with the various biopsy targets were performed successfully in both the laboratory and MRI settings. The proposed biopsy phantoms offered tissue-like signal in MRI and good haptic feedback during needle insertion.

Conclusions: The proposed methods could be valuable in the process of validating the accuracy of MRI-guided biopsy robotic devices in both laboratory and real environments.

KEYWORDS
agar phantoms, breast biopsy, motion accuracy, MRI-guided, needle targeting, robotic device

1 | INTRODUCTION

Percutaneous needle biopsies constitute an alternative to surgical biopsies offering reduced invasiveness and faster recovery.[1,2] Over the years, technological advances have led to the increasing adoption of robotically assisted image-guided percutaneous biopsies over traditional biopsy, which is based on manual needle insertion by the radiologist.[1,2] The superior stability and precision of robotic manipulators compared to human hands have enabled more reliable biopsy procedures. Ultrasound (US), Magnetic resonance imaging (MRI) and

computed tomography are typically employed for localising the suspicious lesion and guiding the needle manipulator based on image feedback.[1,2] Robotically assisted biopsy has been introduced in multiple organs including the lung,[3] breast,[4] prostate,[5] liver,[6] etc.

Breast cancer is the most common form of cancer malignancy in women and the fifth cause of cancer-related death worldwide.[7,8] Diagnosis at an early stage provides patients with the best management and increased survival rates. Following clinical examination and imaging assessment, percutaneous biopsy is required for lesions suspicious for malignancy.

US is the modality of choice for image-guided biopsy of soft lesions that are visible on the US and is usually performed free-handed using core biopsy sampling.[9] Various robotic systems[10–13] for US-based needle guidance have been developed at the experimental level through the years to facilitate doctors.[14] Stereotactic mammography guidance is usually the gold standard for tumours that are not visible on US images, such as microcalcifications. Accordingly, there are several commercially available robotic mechanisms for needle alignment under the specific modality.[15,16]

MRI is increasingly being used as the guidance modality for breast biopsy, especially for women with a high risk of breast cancer.[17] Since small lesions may not be detectable with the standard methods,[18] MRI-guided biopsy is needed to histologically determine the possible malignancy of the tumour. A wide variety of robotic systems that can be utilised in combination with an MRI scanner for automatic positioning of the needle have been developed so far,[4,19–21] thus addressing the requirement to move the patient out of the scanner multiple times and pointless acquisition of a large tissue volume, as well as reducing the procedure duration. These systems address challenges regarding safe operation of robotics in the MRI environment.

Such robotic-assisted approaches require high accuracy and precision in order to reach a target with minimal invasion and fulfil the clinical requirement. All methodologies for testing a robot's mechanical accuracy as well as the accuracy and repeatability of positioning a biopsy needle are based on comparing the intended with the actual motion step as determined using a distance-measuring method.[22,23] Before a process can be implemented in *in vivo* applications, its accuracy is typically assessed in free space, also known as the intrinsic system accuracy. Following demonstration of appropriate motion accuracy and repeatability through benchtop testing, the system should be employed in the real environment (e.g., an MRI system) to ensure that a high level of accuracy is maintained.[22]

Several motion tracking methods were employed in the context of evaluating the targeting accuracy in benchtop experiments.[20,24–28] Optical tracking devices have been frequently utilised in this regard, where the error of positioning was defined as the divergence of the actual from the intended location of the needle tip.[20,24–26] As an example, a robot designed for breast biopsy was tested by navigating a rigid tool to reach target positions following both straight and curved pathways and tracking its motion using an optical tracker.[20] A similar approach was followed in a study by Groenhuis et al.,[4] in which the needle positioning accuracy of a robot proposed for breast biopsy was tested in free air utilising a board with multiple crosshairs, which served as the targets. The needle tip was instructed to puncture these targets, and the positioning error was calculated by measuring the distance between the centre of each target and the respective punched hole.[4]

High-quality breast biopsy phantoms constitute a valuable tool in needle biopsy training and experimentation, as well as in testing the needle positioning accuracy of robotic-assisted biopsy devices. Commercially available breast biopsy phantoms are composed of patented realistic and durable breast tissue with several types of masses of varying sizes interspersed randomly throughout them.[29–32] Membranes mimicking the skin are utilised to cover the tissue, providing realistic needle resistance to trainees.[29–32]

Not only commercially available, but also 'laboratory' phantoms have been proposed over time for biopsy training purposes. In fact, many institutions preferred home-made alternatives for their studies, utilising food or animal products, since they are low cost and easy to make. Turkey or chicken breast, as well as gel-based tissue-mimicking phantoms are commonly used to simulate soft tissue.[33] The inserts could be of liquid or solid content depending on the type of biopsy procedure that will be followed. For freehand US-guided breast biopsy training, raw materials including olives with pimentos, grapes, capers, strawberries, peas and potatoes have been proposed in the literature as tumour mimics.[33]

Household and raw materials were also utilised for mimicking lesions in Magnetic Resonance (MR)-compatible breast phantoms. In that case, the success of the biopsy procedure can be confirmed directly by visualisation of the tumour material in the obtained sample[34] or through MRI by the location of the needle or the created void in relation to the target on intra-operative or follow up MRI images.[35] For instance, Werner et al.[34] assessed the reliability of an MRI-guided biopsy procedure in agarose phantoms containing peas, where the biopsy success was defined as the visual inspection of the specimen. Similarly, the accuracy of an automated system designed for lesion localization while operating at the MRI isocenter was demonstrated in a grapefruit phantom, in which the artificial lesions were vitamin E capsules,[36] by checking whether the capsule material was contained in the specimen chamber. Schneider et al.[35] also assessed an MRI-guided breast lesion localization system in a grapefruit-based phantom, in which breast tissue was mimicked by a grapefruit and the tumour by an embedded long wooden dowel. The success of the procedure was defined by whether pieces of the wooden dowel were contained within the sample, as well as from the void showed up on follow-up MRI.[35]

Polyvinyl-alcohol cryogel (PVA-C) was also utilised to imitate the breast tissue in MRI-guided biopsy procedures.[4,37,38] The benefits of PVA-C include its robust mechanical properties,[39] as well as its ability to mimic the acoustic and MR relaxation properties of human tissue, and thus, to offer realistic visualisation on both MRI and US.[37] An indicative example is a study by Groenhuis et al.,[4] in which the 'Stormram 4' breast biopsy robotic system was tested by phantom studies in the MRI environment. Breast-shaped phantoms were manufactured by pouring Polyvinyl Chloride (PVC) mixtures into

3D-printed dedicated moulds.[4] Lesions with a size varying from 5 to 20 mm were simulated by fish oil capsules or pieces of stiff PVC added in the phantoms during the cool-off procedure. Various phantom sites were targeted by the needle based on pre-operative MR images and the error was estimated by the offset between the targeted site and reconstructed needle position. Following insertion, the needle was clearly visualised in MRI scans as a hole in the phantom.[4]

Gel phantoms based on agar and gelatin have been proposed as a valuable cost-effective tool in the process of breast biopsy training under ultrasound needle guidance too.[40] In this effort, a recent study presents the development of an agar-based phantom mimicking breast, whose Young's modulus and acoustic properties were tuned to match those of fat, glandular and tumour tissues, thus providing realistic haptic feedback and US visibility during needle insertion.[41] A double-layered gelatin-based phantom with simulated tumours have been recently proposed for similar purpose in another study.[33] Interestingly, a glove finger filled with coloured solution served as a cyst, whereas the benign and malignant tumours were simulated by plant-based raw materials.[33]

Agar phantoms could also constitute a valuable testing tool for MRI-guided robotic-assisted biopsy systems and protocols, mainly owing to its tissue-like MRI properties.[42–48] In fact, agar gels are predominantly chosen for MRI phantom studies because they can generate tissue-like MRI signal[42] and replicate the MR relaxation properties of different types of soft tissue upon addition of proper concentration of supplementary ingredients.[49] Furthermore, MRI phantoms are typically employed in the process of MRI safety testing of such devices,[50] which is required before the accuracy and precision of needle targeting can be actually tested in the real environment. Of note, Gadopentetate dimeglumine (Gd-DTPA); a commonly used contrast agent for MR imaging,[51] can be added in gel-based lesion mimics to improve the MRI contrast with respect to the surrounding breast tissue-mimicking material.[52]

Either commercially available or home-made phantoms utilising household raw and laboratory materials are of great use in testing the performance of robotic-assisted breast biopsy devices and procedures. Herein, we propose some simple and cost-effective methods for testing MRI-guided breast biopsy robotic devices in terms of the accuracy of mechanical motion and needle targeting in both laboratory and MRI settings. In-house made dedicated phantoms containing agar as the gelling agent and biopsy targets served as the main tool in the evaluation process. An MRI compatible 2-degrees of freedom (DOF) positioning device developed previously by our group was utilised in all the experiments.[53] Signal to noise ratio (SNR) experiments were initially carried out to confirm the safe and proper operation of the system in a 3T MRI scanner. Planning for needle navigation relative to the target was performed on MRI images utilising the tools of a custom-made biopsy software. Laboratory evaluation of the needle targeting accuracy was based on a repeatability phantom test and a laser based-method. The accuracy of needle targeting was then assessed by MRI phantom studies.

2 | MATERIALS AND METHODS

2.1 | Robotic positioning device

A positioning system previously developed by our group was employed for the purpose of the current study.[53] The system was manufactured on a 3D printing machine (FDM400, Stratasys) using Acrylonitrile Butadiene Styrene thermoplastic. The positioning mechanism features two DOF with a 6 cm motion range each, which are driven by piezoelectric motors (USR30-S3, Shinsei Kogyo Corp.) while motion feedback is provided by optical encoders (EM1-0-500-I, US Digital Corporation). The mechanical components were enclosed within a compact enclosure, resulting in the development of the device shown in Figure 1. As shown in the computer-aided design drawing of Figure 1A, a needle holder served as the end effector of the device extending from the mechanism through an arm.

The robotic device was designed based on two main requirements: (a) MRI compatibility and (b) highly accurate motion and needle positioning. In terms of MRI compatibility, the robot's materials and mechatronic components were carefully selected to ensure no interference with the scanner and safe operation of the robot in the MRI bore. A dedicated design is also required for the robot to fit the scanner while leaving sufficient space for comfortable patient placement, given the restricted space of the bore. The compact dimensions of the device of 40 cm in length, 15 cm in width and 7 cm in height enable its placement inside the MRI scanner between the subject and the bore for lateral approach of the needle, as shown in Figure 1A,B. Regarding the second requirement, the targeting accuracy should be sufficiently high for targeting early stage cancer with the required precision and accuracy. A detailed description of the system design and manufacturing can be found in the study by Drakos et al.[53]

2.2 | Needle navigation software

Navigation software integrating commands for MRI interfacing and robotic positioning control was interfaced with the robot for the purpose of the study. The software includes tools for navigation planning on pre-operative MR images and automatic positioning of the biopsy needle relative to the target area in the *X-Y* plane (robot coordinates). Figure 2A is a screenshot of the software interface for navigation planning.

An image-based registration approach involving the use of a water-filled syringe was followed to pre-operatively register the robot's workspace to the MRI coordinates. The robot is initially secured laterally to the subject and adjacent to the region of interest (ROI) with the needle supporter at its home position. A water-filled syringe was attached to the needle supporter to facilitate registration. Two parallel sagittal scans are acquired at the level of the syringe and subject/phantom, as shown in Figure 2B. Pre-operative images are directly transferred to the dedicated navigation software, thus transferring the planning to the robot's coordinate system. The user defines the desired target on the subject's image and the software

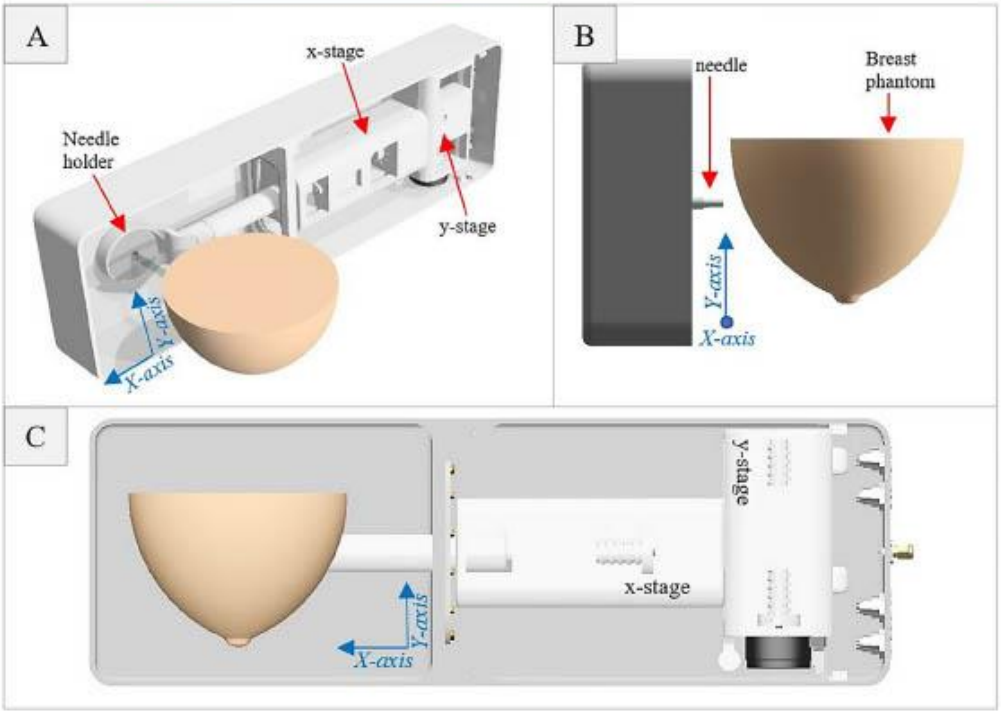

FIGURE 1 Computer-aided design drawings of the robotic device with the breast phantom within the robot's workspace: (A) isometric view showing the motion stages and the needle holder, (B) side view, and (C) front view.

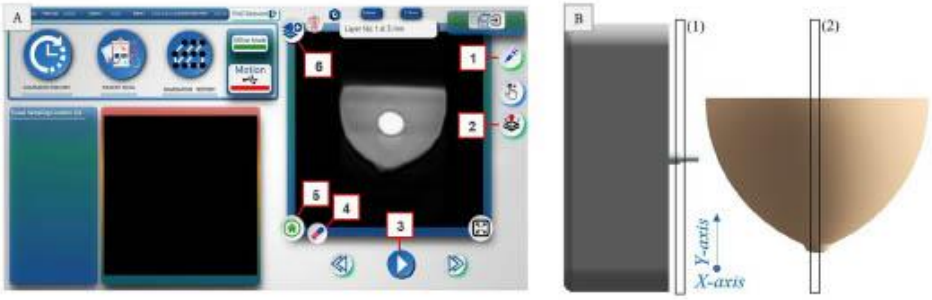

FIGURE 2 (A) Screenshot of the software interface for navigation planning showing the main tools: (1) draws navigation points, (2) manual motion control, (3) starts navigation planning process, (4) erases all navigation points, (5) 'Homing' menu, and (6) creates a new layer. (B) Side view of the device and phantom indicating the location of the sagittal slices at the level of the needle (1) and cherry tomato in the phantom (2).

automatically extracts the motion vectors defining the two-dimensional path of the needle supporter.

Communication with the mechatronic parts of the positioning mechanism is achieved through the electronic driving system located outside the MRI room through shielded cables. The extracted motion commands are thus sent to the electronic driving system for execution so that the syringe moves from its initial position to align with the target location (in a sagittal plane). Therefore, the entire procedure is conducted remotely in the control room, thus streamlining the biopsy process and increasing the overall efficiency. Figure 3 illustrates a hardware wiring diagram indicating the connection and flow signal among components.

2.3 | Agar-based biopsy phantoms

Phantoms simulating breast and tumour tissue were developed to be utilised as the main tool for evaluating the positioning device in terms of MRI compatibility and targeting accuracy. The main requirements for the phantoms were (a) suitability for MRI, (b) tissue-like MRI

appearance, (c) excellent delineation of tumour mimics, and (d) proper stiffness both in terms of achieving reusability and providing tissue-like haptic feedback to the user during needle insertion. Agar was selected as the main ingredient of the phantoms considering the low cost and ease preparation of agar gels as well as their ability to emulate critical properties of various body tissues, including MRI properties.[42]

A single-target breast-shaped phantom was prepared by embedding a cherry tomato in pure agar (Merck KGaA) gel of 4% weight per volume (w/v) concentration. The realistic shape of the phantom was achieved by pouring the agar mixture into a dedicated 3D-printed mold having a breast-shaped cavity. Figure 4A,B show photos of the developed phantom. Figure 4C shows a T2-Weighted (T2-W) Turbo Spin Echo (TSE) image of the phantom. Image acquisition was performed utilising the following parameters: Repetition time (TR) = 2000 ms, Echo time (TE) = 24 ms, Field of view (FOV) = 200 × 200 mm^2, Slice thickness = 10 mm, Matrix size = 128 × 128, Number of averages (NEX) = 1, Echo train length (ETL) = 16, Flip angle (FA) = 180°, and Pixel bandwidth (PB) = 200 Hz/pixel. Note that tomatoes have high water content and thus appear brighter with excellent contrast from the surrounding agar-based material in T2-W TSE imaging.

A multiple-tumour phantom having a square shape and six embedded cylindrical targets of 10 mm in diameter was created by molding in a specially designed mold. Two agar mixtures with notable difference in the MRI relaxation times were prepared to mimic tumour and breast tissue. The concentration of materials for each phantom compartment was selected taking into consideration the T1 and T2 relaxation times of various agar/silica mixtures as measured in a previous study of our group,[49] in order to achieve good MRI contrast. Specifically, an agar gel was prepared using 6% w/v agar and 2% w/v silicon dioxide powder (Sigma-Aldrich) to mimic breast tissue, whereas another mixture of 6% w/v agar and a higher silica concentration of 6% w/v was prepared to mimic tumour tissue. Figure 5A shows a cross section view of the phantom, whereas Figure 5B shows a T2-W MR image of the phantom acquired with the following parameters: TR = 2500 ms, TE = 48 ms, FOV = 200 × 200 mm^2, Slice thickness = 10 mm, Matrix size = 320 × 320, NEX = 1, ETL = 16, FA = 180°, and PB = 50 Hz/pixel. Note that the slight difference in material content resulted in excellent MRI contrast between the tumour mimic and surrounding tissue.

2.4 | Motion accuracy assessment

The accuracy of motion in the *X*- and *Y*-axes was evaluated using a digital calliper with a measuring resolution of 0.1 mm, which was

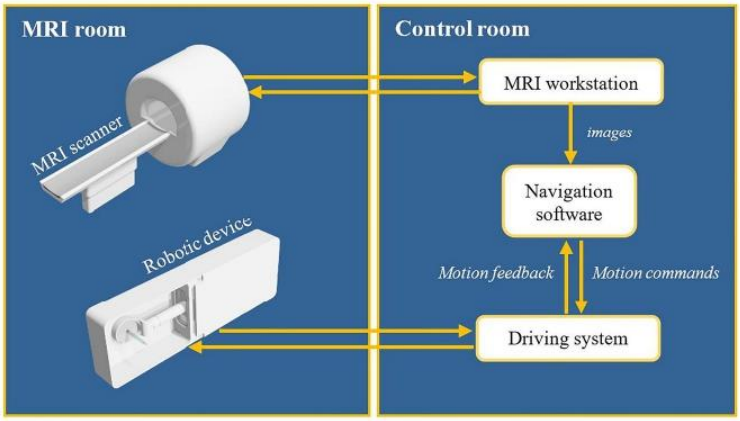

FIGURE 3 Hardware wiring diagram indicating the connection and signal flow among components.

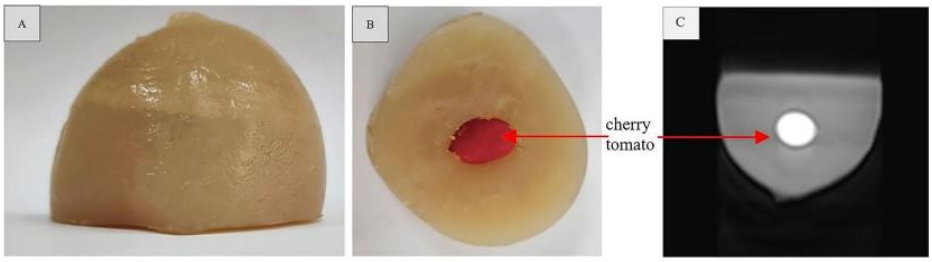

FIGURE 4 Photos of the agar-based phantom containing a cherry tomato: (A) whole phantom and (B) cross-sectioned phantom. (C) Axial T2-W Turbo Spin Echo coronal image of the phantom containing a cherry tomato.

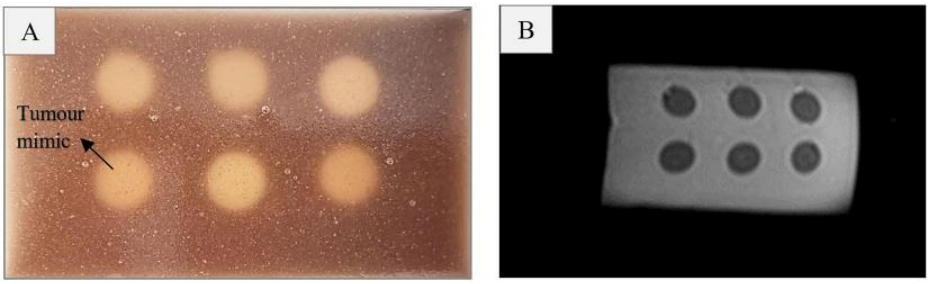

FIGURE 5 (A) Photo of the agar-based phantom with six similar agar-based biopsy targets. (B) T2-W Turbo Spin Echo image of the phantom.

mounted on the motion stage under evaluation using specially designed 3D-printed supports. Bidirectional motion steps of 1, 5, 10 and 40 mm were commanded through the controlling software in both axes and directions. The actual displacements as measured by the calliper's incremental distance were then compared to the commanded (intended) steps to estimate the movement error.

2.5 | MRI compatibility assessment

The next step in the evaluation process was to access the MRI compatibility of the robotic system. The experiment was carried out at the premises of the Germany Oncology Centre in a 3T MR scanner (MAGNETOM Vida, Siemens Healthineers). The assessment was based on SNR measurements in the breast-shaped phantom under the following activation states of the electronic driving system: (a) cables disconnected and DC OFF, (b) cables connected and DC OFF, and (c) cables connected and DC ON. For SNR calculation, the mean signal intensity ($n = 5$) in a single circular ROI set within the breast-shaped phantom ($SI_{phantom}$) was divided by the standard deviation from the relevant ROI defined in air (σ_{noise}) as follows:[54]

$$SNR = SI_{phantom}/\sigma_{noise} \quad (1)$$

In each case, the phantom was positioned at the isocenter of the magnet (0,0) and the signal was calculated as the average intensity in a circular ROI of 5 mm diameter, which was consistently placed at the same location in the phantom/air at a specific distance away from the coil, thus avoiding inhomogeneities due to inconsistent coil placement.

For each activation state, MR axial images were acquired with a Fluid-attenuated Inversion Recovery (FLASH) sequence (TR = 25 ms, TE = 10 ms, FOV = 280 × 280 mm^2, Slice thickness = 6 mm, Matrix size = 128 × 128, NEX = 1, ETL = 1, FA = 30°, PB = 240 Hz/pixel), as well as with a T2-W SE sequence (TR = 2000 ms, TE = 24 ms, FOV = 200 × 200 mm^2, Slice thickness = 10 mm, Matrix size = 128 × 128, NEX = 1, ETL = 16, FA = 180°, PB = 200 Hz/pixel) utilising a multi-channel body coil (18-channel, Siemens Healthineers).

2.6 | Needle targeting accuracy

2.6.1 | Benchtop evaluation

Repeatability phantom test

The purpose of this experimental part was to assess both the accuracy and repeatability of needle targeting in a developed phantom containing a cherry tomato, which served as the target. Figure 6 illustrates the experimental setup arranged in the laboratory. The device was interfaced to the laptop with the relevant biopsy software through the custom made electronic driving system and the breast phantom was securely mounted on a dedicated holder within the robot's workspace, allowing for easy access of the needle. A 3D-printed needle made out of Acrylonitrile Styrene Acrylate thermoplastic of 3-mm in diameter was utilised. Once the needle was placed at the location determined by the software coordinates (in *X*-*Y* robot coordinates), it was manually inserted in the phantom to puncture the target. The success of the procedure was visually assessed by checking whether the plastic needle pierced the cherry tomato. Needle navigation was performed 10 times to check the repeatability. Before each repetition, the needle holder was commanded to return to its home position.

Laser based method

The current experiment was carried out in another laboratory setting involving the use of a plastic grid instead of a phantom. The needle was replaced by a laser pointer (HY3003, Mastech DC Power Supply), which was navigated in the two PC-controlled axes (*X* and *Y*) to target preselected cells of the plastic grid shown in Figure 7A. The cells had dimensions of 2 × 2 mm^2, and the thickness of the grid lines was 1 mm. The user selected a random cell on the relevant pre-obtained MR image of the grid, as shown in the software screenshot of Figure 7B. The laser pointer was then automatically positioned according to the extracted software coordinates and the success of the procedure was determined by the offset between the location of the red light of the laser pointer and the target position as set in the software. The exact position of the red light was estimated by measuring the cells from the origin point in the *X*- and *Y*-axes and translating them to distance in mm. Overall, 20 grid cells were randomly selected and visited.

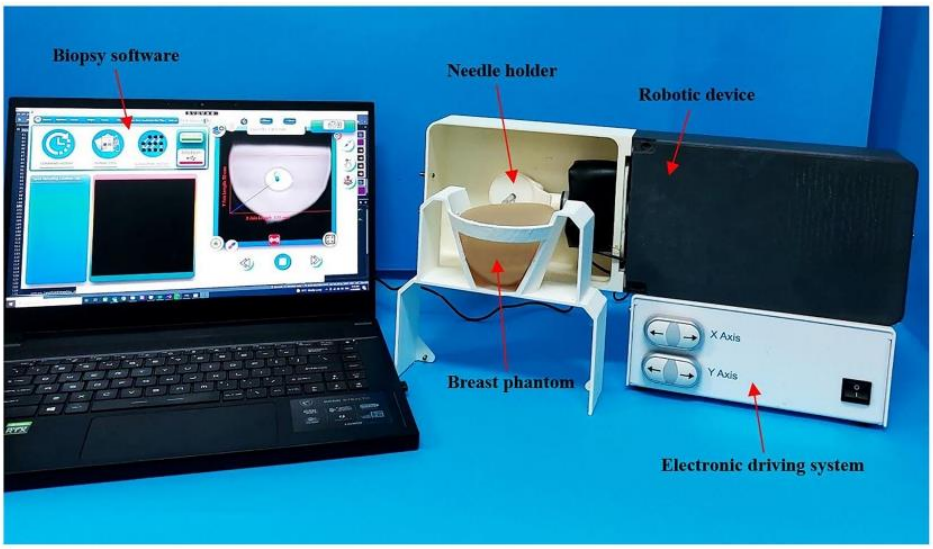

FIGURE 6 Photo of the experimental setup arranged in the laboratory for the assessment of the needle targeting accuracy.

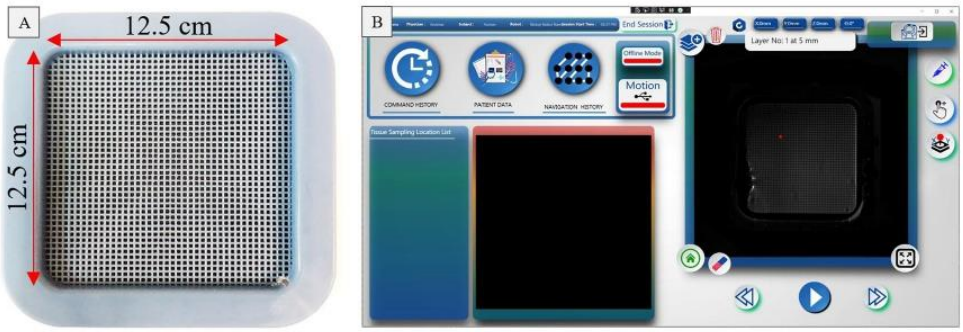

FIGURE 7 (A) Plastic grid utilised for the laser-based technique. (B) Screenshot of the software interface for navigation planning on the magnetic resonance imaging image of the grid.

2.6.2 | MRI evaluation

The targeting accuracy of the biopsy needle was then assessed by MRI. The experiment was carried out in a 3T MR scanner (MAGNETOM Vida) utilising the in-house made agar-based phantoms. The robotic device was securely placed on the MRI couch with the breast-shaped phantom fixed on the dedicated holder used for benchtop evaluation (Figure 6), and covered by the 18-channel body coil (Siemens Healthineers) with the assistance of a dedicated plastic positioner. A water-filled syringe was attached to the needle holder of the robot.

Images were acquired at the level of the syringe and phantom, as shown in Figure 8, using a T2-W SE sequence with the following parameters: TR = 2000 ms, TE = 24 ms, FOV = 200 × 200 mm^2, Slice thickness = 10 mm, Matrix size = 256 × 256, NEX = 1, ETL = 16, FA = 180°, and PB = 200 Hz/pixel, to determine the desired coordinates of the syringe. The syringe was robotically moved along the planned path to coincide with the selected location within the cherry tomato in the sagittal plane (*X-Y* plane in robot coordinates). Following positioning of the syringe, T2-W images (with the above-mentioned parameters) were acquired and fused to visualise the syringe position relative to the cherry tomato. Once confirming proper positioning, the syringe was replaced by a needle that was manually inserted in the phantom to puncture the target. Again, T2-W images were acquired for assessing the targeting accuracy.

A similar planning procedure was followed for the multiple-tumour model, in which a specific tumour target was randomly selected by the user through the software. After motion execution and manual needle insertion, image acquisition was performed with a T1-Weighted (T1-W) TSE sequence with the following parameters: TR = 700 ms, TE = 23 ms, FOV = 280 × 280 mm^2, Slice thickness = 10 mm, matrix size = 128 × 120, ETL = 6, NEX = 2, FA = 30°, and PB = 50 Hz/pixel, to detect the needle location relative to the targeted tumour mimic.

3 | RESULTS

3.1 | Motion accuracy assessment

The measured range of actual displacement for each commanded distance (1, 5, 10, and 40 mm) in both the *X*- and *Y*-axes is listed in Table 1. Figure 9 shows the mean-measured distance ($n = 20$) versus the intended distance for the *X*-axis right and left directions, while Figure 10 shows the corresponding graph for the *Y*-axis upward and downward directions. The results indicate a maximum error of 0.1 mm for linear motion steps of up to 10 mm, whereas a two-times larger maximum error was observed for the motion step of 40 mm.

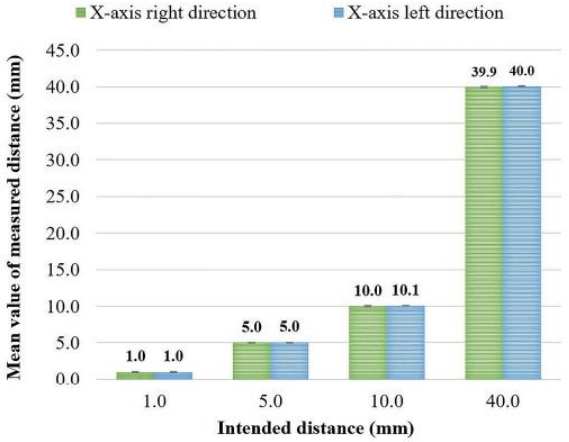

FIGURE 9 Mean value of measured distance plotted against the intended distance for the *X*-axis in the right and left directions. Error bars represent the standard deviation of the mean.

3.2 | MRI compatibility assessment

MRI compatibility was assessed by comparing the SNR of phantom images acquired at various activation conditions of the electronic

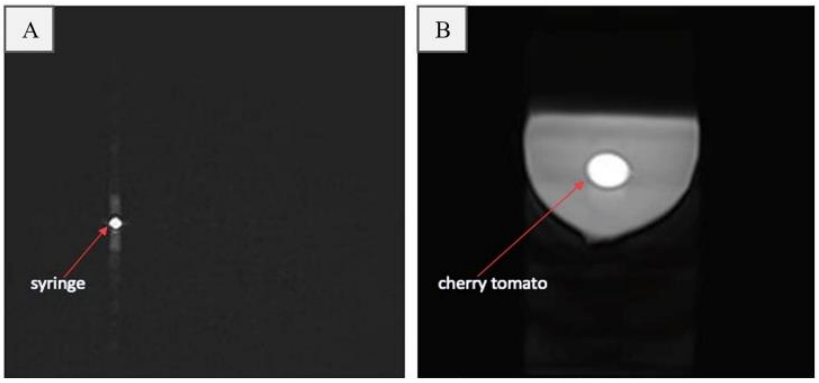

FIGURE 8 Sagittal T2-W images showing (A) the water-filled syringe located at its initial position, and (B) the breast-shaped agar-based phantom featuring a cherry tomato.

TABLE 1 The measured range of actual displacement for each commanded distance (1, 5, 10, and 40 mm) in the *X*- and *Y*-axes for 20 repetitions.

Intended motion step (mm)		1.0		5.0		10.0		40.0	
Y-stage		Upward direction	Downward direction	Upward direction	Downward direction	Upward direction	Downward direction	Upward direction	Downward direction
	Range of measured distance (mm)	0.9–1.1	0.8–1.1	4.9–5.1	4.9–5.1	9.9–10.1	9.9–10.1	39.9–40.1	39.8–40.0
X-stage		Right direction	Left direction	Right direction	Left direction	Right direction	Left direction	Right direction	Left direction
	Range of measured distance (mm)	0.9–1.1	0.9–1.1	4.9–5.1	5.0–5.1	9.9–10.1	10.0–10.1	39.8–40.1	39.8–40.0

driving system, as shown in Figures 11 and 12. Specifically, Figure 11 shows the axial 2D FLASH and T2-W SE images acquired at each tested state. A bar chart of the relevant SNR measurements for both tested sequences is shown in Figure 12.

3.3 | Needle targeting accuracy

3.3.1 | Benchtop evaluation

Regarding the repeatability test, the needle pierced the targeted tumour successfully in all 10 repetitions. Furthermore, there was a very good agreement in the location of the needle tip among repetitions. An indicative photo showing the punctured tomato is shown in Figure 13. Figure 14 shows indicative results of the laser-based experiment, where a randomly selected cell located at the lower

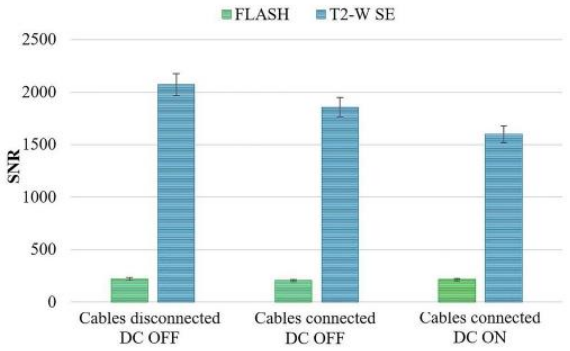

FIGURE 12 Bar chart of the signal to noise ratio measured at different activation states of the electronic driving system using FLASH and T2-W SE sequences.

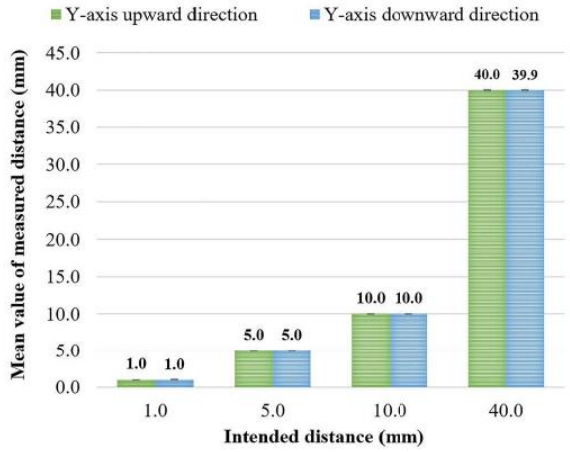

FIGURE 10 Mean value of measured distance plotted against the intended distance for the Y-axis upward and downward directions. Error bars represent the standard deviation of the mean.

FIGURE 13 Photo of the phantom showing the needle tip location after motion execution and needle insertion in the cherry tomato. Arrow indicates the plastic needle.

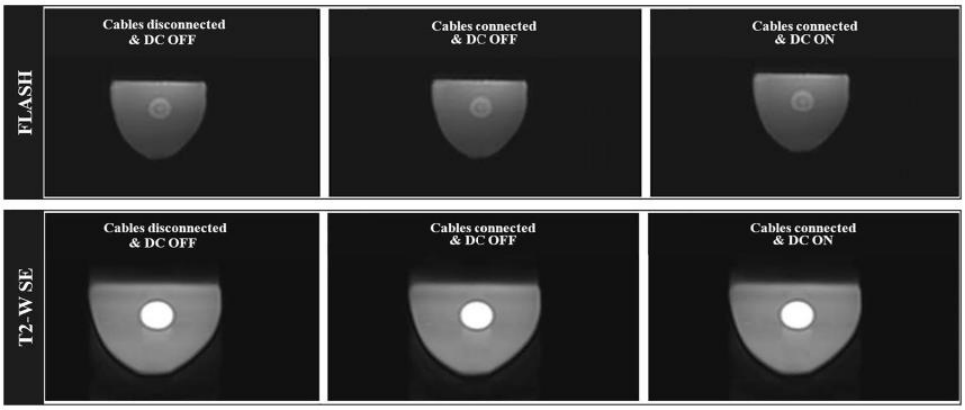

FIGURE 11 Axial 2D FLASH and T2 W SE images of the breast-shaped agar-based phantom acquired at different activation states of the electronic driving system.

right of the grid was targeted. The results of the actual (measured) and software coordinates for all visited cells ($n = 20$) showed a mean targeting error of 1 mm in both the *X*- and *Y*-axes.

3.3.2 | MRI evaluation

Typical results of the needle targeting accuracy in the MRI setting are presented in Figures 15 and 16. After localization and placement of the syringe relative to the cherry tomato, T2-W sagittal SE images at the level of the syringe and the phantom were fused into the image of Figure 15A, which confirmed successful placement. The syringe was aligned with all the tumour mimics successfully, with a maximum offset between the commanded and actual syringe tip location of 1 mm. Successful puncture of the tumour was followed in all cases by manually advancing the needle. Figure 15B shows a T2-W SE image acquired after needle insertion, where the needle tip is visualised as a spot of reduced intensity within the tomato.

Figure 16 shows indicative results of the experiment carried out in the multiple-tumour phantom model, where the middle bottom tumour mimic was targeted. After motion execution and manual needle insertion, the needle tip was clearly visualised within the target in the T1-W SE image of Figure 16A without any noticeable susceptibility artefacts. Figure 16B is a photo of the punctured phantom.

4 | DISCUSSION

In the current study, we aimed to share our experience in assessing the motion and needle targeting accuracy of a biopsy positioning device through simple and inexpensive benchtop and MRI

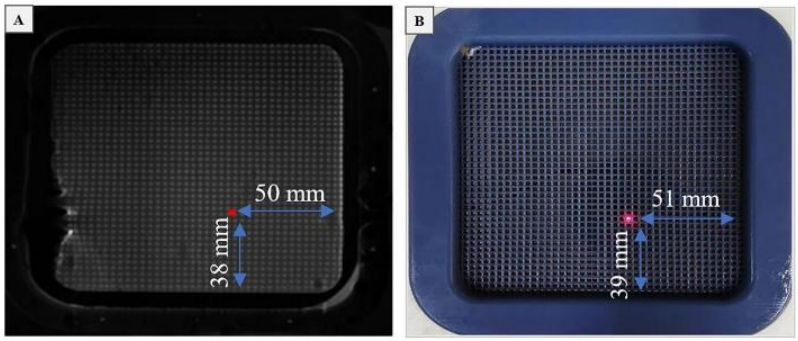

FIGURE 14 (A) Random grid cell selected on the software. (B) The laser location after motion execution.

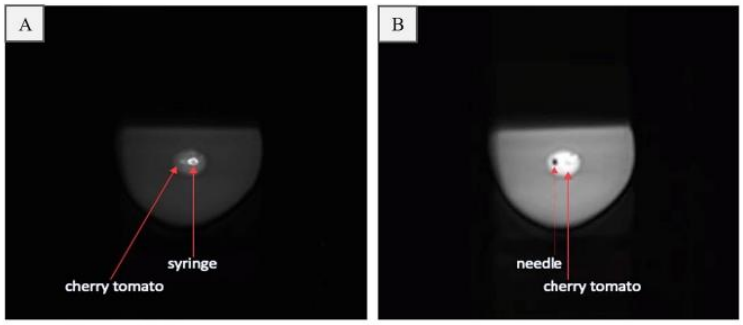

FIGURE 15 (A) Fused sagittal T2-W SE images showing the location of the water-filled syringe relative to the cherry tomato. (B) Sagittal T2-W SE image showing the needle as inserted in the cherry tomato.

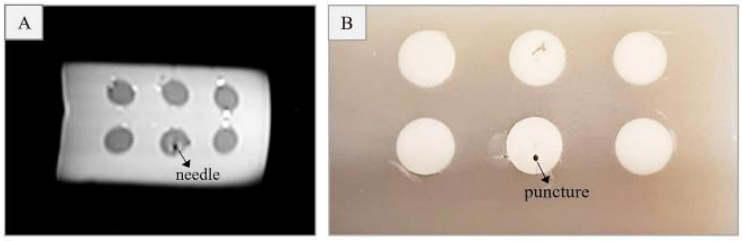

FIGURE 16 (A) T1-W SE image of the phantom featuring six agar-based tumour mimics after needle targeting. (B) Photo of the punctured phantom.

experiments. For this purpose, an MRI compatible positioning device featuring two DOF that was previously developed by our group[53] was equipped with a dedicated holder serving as the end-effector of the mechanism to accommodate a 3D-printed plastic needle of 3-mm diameter. The motion accuracy of the two mechanical stages offering motion in the *X*- and *Y*-axes was assessed by a benchtop calliper-based methodology, whereas in-house made phantoms mimicking both breast and tumour tissue served as the main tool for evaluating the accuracy and repeatability of needle targeting. A custom-designed MRI-guided biopsy software allowed navigation planning on pre-procedural MR images for manoeuvring the needle holder relative to the ROI.

The first step in the evaluation process concerned the motion accuracy of the two linear motion stages (*X* and *Y*) in the benchtop setting. The maximum error of linear motion for motion steps of up to 10 mm in the *X*- and *Y*-axes was estimated at 0.1 mm, thus demonstrating a highly accurate mechanical motion in both axes. High accuracy and repeatability of robotic motion in the free field is required so that sufficient accuracy in the real environment where other sources of error are present is maintained. Notably, the described calliper-based methodology is considered universal since it could be used for assessing the motion accuracy of any positioning biopsy or therapeutic device provided that its design is appropriate.

Two phantom models containing biopsy targets were created using agarose as the main ingredient to assess the biopsy device in terms of MRI compatibility and needle targeting accuracy. Both phantoms offered tissue-like signal in MRI and realistic haptic feedback, that is, a realistic haptic feeling for users throughout the needle insertion procedure (soft-tissue like density). SE imaging yielded phantom images of very good quality in terms of resolution and contrast between tumour mimics and surrounding tissue (Figures 4 and 5). It is now generally accepted that agar phantoms can provide a tissue-like signal in MRI.[42] In this study, a cherry tomato was selected as the first target since it has high water content appearing brighter than the surrounding tissue, whereas the MRI appearance of the agar-based tumour mimics was differentiated from the surrounding by adding a higher silica concentration. Notably, in case a fine-needle aspiration or a core biopsy needle will be utilised instead, the breast shaped phantom embedding a cherry tomato will allow for direct confirmation of the success of the sampling procedure through the visualisation of tomato pieces within the sample.

According to the tumor, nodes, and metastases classification for clinical breast cancer staging, invasive breast tumours are categorised into stages 1 through 4.[55] In terms of size, the first stage (T1) concerns tumours that are 20 mm or smaller in size at their widest area.[55] In this study, the authors selected a cherry tomato of almost 20 mm in diameter, whereas the agar-based tumour simulators had a smaller diameter of 10 mm. Therefore, the tumour models used can be considered representative of T1 stage tumours at least in terms of size. Although simplified tumour models of spherical/ellipsoid shape were employed in the study, one could easily create tumour models of a more complex shape using 3D printed dedicated molds.

Before assessing the system's accuracy in the real environment, its compatibility with a 3T MRI scanner was assessed. In general, according to the American Society for Testing and Materials standards (F2503), the system is classified as 'MR conditional' because electricity is required for its operation. In this study, MRI compatibility was defined as the ability of the system to operate in the MRI environment without significantly affecting the quality of diagnostic and monitoring information and was tested by comparing the SNR in the breast phantom among different activation conditions of the electronic driving system. Of note, the SNR is a typical metric in the context of MRI compatibility assessment of robotics.[54,56,57] The SNR in the presence of the robotic device in a passive mode (cables disconnected) served as the reference value since it was similar to that obtained using the phantom alone (mounted on the patient table). In fact, an SNR reduction in the order of 2.5% occurred in the presence of the device, which was considered insignificant in terms of the resultant image quality.

According to the results, the SNR of FLASH images was minimally affected by changes in the activation mode varying in the range of 205–220. The employed T2-W SE sequence yielded 7- to 9-fold higher SNR values than the FLASH sequence depending on the examined activation state. The SNR of T2-W SE images was reduced by approximately 25% upon connection and activation of electronics compared to the reference value (device present but deactivated). However, it remained at a satisfactory level for high-quality imaging, thus demonstrating the suitability of the positioning system for the purposes of the study.

It is worth discussing that the presence of the robotic device in the MRI scanner can lead to various susceptibility artefacts. Motion actuators and encoders may contain magnetic materials that perturbate the magnetic field homogeneity causing signal dephasing and faults in the image readout process, thus resulting in areas of signal loss (appear hypointense) and distortion phenomena.[58] Accordingly, some geometric distortion occasionally observed on MRI images (Figures 14 and 16) can be attributed to magnetic field inhomogeneities. However, it was only present at the edges of the imaged objects and did not prevent the successful targeting and puncture of the various tumour mimics. At this point, it is essential to mention that there have been proposed some measures to minimise such susceptibility phenomena in previous literature.[54]

Benchtop experiments were then carried out to assess the ability of the biopsy needle to reach targets with the required precision and accuracy. A repeatability test was carried out in the laboratory setting, where the needle was repetitively commanded ($n = 10$) to align with the location of the cherry tomato in the breast-shaped phantom (in *X*-*Y* vertical plane) while needle insertion was performed manually. In all repetitions, the needle pierced the tumour mimic successfully at the exact location defined by the software, with excellent agreement in the location of the needle tip among repetitions. Regarding the laser-based approach, a mean targeting error of 1 mm was estimated for the *X*- and *Y*-axes, thus providing additional evidence of highly accurate needle positioning.

Although simple and straightforward, this method has the limitation that it can only provide results with a mm resolution.

Needle navigation relative to the developed biopsy phantoms was also performed successfully in the MRI setting without any reported mechanical malfunction. The method involved the use of a water-filled syringe which was navigated to align with the location of a tumour mimic (in *X*-*Y* robot coordinates), which was then punctured by manually pushing the needle forward. The needle tip was clearly visualised within the target in follow-up T1-W and T2-W SE images with minor susceptibility artefacts. Remarkably, a small offset between the position of the syringe and needle was observed in the MRI scans and was attributed to the error introduced by the user. These results further demonstrated that the system maintains accurate positioning when operated in the real environment and could be utilised for image-guided robotic-assisted biopsy procedures.

The robotic system employed in the study was designed in a simplified and ergonomic manner for lateral needle approach, thus avoiding accidental interaction with the ribs. The positioning mechanism allows needle navigation in a single plane perpendicular to the needle insertion direction (*X*-*Y* plane in robot coordinates and sagittal place in MRI coordinates) followed by the user pushing the needle towards the target. This is the typical clinical scenario where the doctor performs final needle insertion, thus maintaining human control. Accordingly, the proposed methods as described herein were designed based on the functionalities of the employed robotic system. However, they can be easily adjusted to suit biopsy systems with more DOF as well as systems allowing angulation. In that case, multi-dimensional planning and probably the incorporation of deep learning methods will be required.

An important question associated with the navigation planning procedure is whether the accuracy of the proposed techniques can be compromised by poor image resolution. In the current study, since navigation planning to align the syringe/needle supporter with the target was limited to the plane of interest, only the in plane resolution was considered to affect the accuracy of results, whereas the slice thickness was not. Therefore, given the size of the syringe (diameter of about 3 mm) and tumour mimics, the voxel size of approximately 0.78 $\times$ 0.78 mm^2 used for image acquisition was considered sufficiently small for proper delineation of the syringe and target and allowed for accurate registration of the needle supporter position relevant to the target. Successful alignment of the syringe with the biopsy targets also confirmed that the motion vectors defining the two-dimensional needle path were accurately extracted. Others could adjust the MRI resolution to the specific features of their biopsy system.

According to the study findings, the mechanical stages of the robot can move in free space with a minimum accuracy of 0.1 mm. When MRI-based needle navigation is involved, other sources of error related to image registration as well as the image quality (e.g., pixel size) may affect the positioning accuracy. In that case, MRI experiments revealed a maximum error of needle positioning of 1 mm, which agrees with the mean positioning error estimated using the laser-based method. In experiments involving puncture of the tumour mimics, the procedure was deemed either successful when the target was punctured or 'unsuccessful' when not. Although all targets were successfully punctured, occasionally, the needle appeared slightly shifted from the desired location, which was attributed to the repeatability error introduced by the user. In other words, while the robotic system is characterised by high accuracy and repeatability of needle positioning in both benchtop and MRI settings, the success of tumour puncture and final needle position are highly dependent on the user's performance.

In this study, the system was able to accurately target tumours of at least 10 mm in their widest area. However, the estimated maximum error of needle alignment with the target of 1 mm suggests that smaller tumours of at least 3 mm in diameter could also be targeted accurately in both benchtop and MRI environments. However, further investigation is required in this regard. Generally, given the high sensitivity of MRI for cancer detection (higher than mammography),[59] very early stage cancer can be detected by MRI and if needed, directly biopsied using the proposed system. Accordingly, upon preclinical validation and acquisition of sufficient evidence demonstrating safe and efficient operation, the system could be translated to the clinical setting for the biopsy of early stage cancer.

Overall, this study aimed to provide a detailed description of several phantom-based methods dedicated to evaluating the targeting accuracy of biopsy robotic devices. The suggested methods are straightforward to implement without special training using easily sourced and cost-effective materials. The developed phantoms are made of inexpensive ingredients that are easily accessible to other researchers. It is noted that gel phantoms are generally considered more ergonomic than phantoms where turkey or chicken breast is used to simulate soft tissue.[33] While there are numerous evaluation methods proposed in the literature, they are typically more complicated and/or require the use of specific equipment. For example, motion tracking methods are commonly employed in the context of evaluating the accuracy of needle positioning,[20,24–28] but they require the use of dedicated equipment, such as optical tracking devices, thus being less cost-effective and ergonomic. At the same time, they cannot be employed in the MRI environment. Overall, the methods proposed herein are considered much simpler, ergonomic, and universal.

5 | CONCLUSIONS

The current study proposes ergonomic and cost-effective methods for assessing the performance of robotic devices intended for MRI-guided needle biopsy in both laboratory and real environments. The in-house made biopsy phantoms offered tissue-like signals in MRI and good haptic feedback during needle insertion. The proposed benchtop and MRI techniques provided useful data regarding the

accuracy and repeatability of robotic motion and needle targeting as well as proper functionality of the biopsy software and integrated navigation algorithms. MRI experiments further allowed us to determine whether highly accurate operation is maintained in the real environment. All methods can be easily implemented without training using easily sourced and cost-effective materials individually or interchangeably to confirm each other. Although the study was focused on breast biopsy, the methods and experience can be expanded for other organs as well.

AUTHOR CONTRIBUTIONS

Anastasia Antoniou contributed to the drafting of the manuscript and scientific methods. Anastasia Nikolaou, Nikolas Evripidou, and Vasiliki Zinonos contributed to the implementation of the experiments. Andreas Georgiou and Marinos Giannakou contributed to the development of the software and robotic device, respectively. Antria Filippou contributed to data analysis. Antreas Chrysanthou and Cleanthis Ioannides contributed to the MRI experiments. Christakis Damianou supervised the overall study, as well as the drafting of the manuscript.

ACKNOWLEDGEMENTS

The project was funded by the Research and Innovation Foundation of Cyprus. The robotic device used for the purposes of the study was developed under the project FUSROBOT (ENTERPRISES/0618/0016), whereas the software development and reported experiments were carried out under the projects SOUNDPET (INTEGRATED/0918/0008) and MRBREASTBIO (CONCEPT/0521/0040).

CONFLICT OF INTEREST STATEMENT

The authors declare no conflicts of interest.

DATA AVAILABILITY STATEMENT

The data that support the findings of this study are available from the corresponding author upon reasonable request.

ORCID

Nikolas Evripidou https://orcid.org/0000-0002-8200-3349
Marinos Giannakou https://orcid.org/0000-0002-6777-0515
Christakis Damianou https://orcid.org/0000-0003-0424-2851

REFERENCES

1. Siepel FJ, Maris B, Welleweerd MK, Groenhuis V, Fiorini P, Stramigioli S. Needle and biopsy robots: a review. *Curr Robot Rep*. 2021;2(1):73-84. https://doi.org/10.1007/s43154-020-00042-1
2. Unger M, Berger J, Melzer A. Robot-assisted image-guided interventions. *Front Robot AI*. 2021;8:1-7. https://doi.org/10.3389/frobt.2021.664622
3. Kratchman LB, Rahman MM, Saunders JR, Swaney PJ, Webster RJ. Toward robotic needle steering in lung biopsy: a tendon-actuated approach. In: *Proceedings of SPIE - The International Society for Optical Engineering*; 2011. https://doi.org/10.1117/12.878792
4. Groenhuis V, Siepel FJ, Veltman J, van Zandwijk JK, Stramigioli S. Stormram 4: an MR safe robotic system for breast biopsy. *Ann Biomed Eng*. 2018;46(10):1686-1696. https://doi.org/10.1007/s10439-018-2051-5
5. Xu H, Lasso A, Vikal S, et al. MRI-guided robotic prostate biopsy: a clinical accuracy validation. *Med Image Comput Comput Assist Interv*. 2010;13:383-391. https://doi.org/10.1007/978-3-642-15711-0_48
6. Schulz B, Eichler K, Al-Butmeh F, et al. Computed tomography guided percutaneous liver biopsy using a robotic assistance device—a corpse study. *Open J Radiol*. 2015;05(02):84-91. https://doi.org/10.4236/ojrad.2015.52014
7. World Health Organization (WHO). Breast cancer. Source: Globocan 2020. Accessed October 11, 2022. https://gco.iarc.fr/today/data/factsheets/cancers/20-Breast-fact-sheet.pdf
8. Momenimovahed Z, Salehiniya H. Epidemiological characteristics of and risk factors for breast cancer in the world. *Breast Cancer Targets Ther*. 2019;11:151-164. https://doi.org/10.2147/BCTT.S176070
9. Apesteguía L, Pina LJ. Ultrasound-guided core-needle biopsy of breast lesions. *Insights Imaging*. 2011;2(4):493-500. https://doi.org/10.1007/s13244-011-0090-7
10. Megali G, Tonet O, Stefanini C, et al. A computer-assisted robotic ultrasound-guided biopsy system for video-assisted surgery. *Lect Notes Comput Sci*. 2001;2208:343-350. https://doi.org/10.1007/3-540-45468-3_41
11. Smith WL, Surry KJM, Mills GR, Downey DB, Fenster A. Three-dimensional ultrasound-guided core needle breast biopsy. *Ultrasound Med Biol*. 2001;27(8):1025-1034. https://doi.org/10.1016/s0301-5629(01)00396-9
12. Abayazid M, Moreira P, Shahriari N, Patil S, Alterovitz R, Misra S. Ultrasound-guided three-dimensional needle steering in biological tissue with curved surfaces. *Med Eng Phys*. 2015;37(1):145-150. https://doi.org/10.1016/j.medengphy.2014.10.005
13. Welleweerd MK, Siepel FJ, Groenhuis V, Veltman J, Stramigioli S. Design of an end-effector for robot-assisted ultrasound-guided breast biopsies. *Int J Comput Assist Radiol Surg*. 2020;15(4):681-690. https://doi.org/10.1007/s11548-020-02122-1
14. Sommerich CM, Lavender SA, Evans K, et al. Collaborating with cardiac sonographers to develop work-related musculoskeletal disorder interventions. *Ergonomics*. 2016;59(9):1193-1204. https://doi.org/10.1080/00140139.2015.1116613
15. HOLOGIC. Affirm breast biopsy guidance system. Accessed October 25, 2022. https://www.hologic.com/hologic-products/breast-health-solutions/affirm-breast-biopsy-guidance-system
16. HOLOGIC. Affirm prone breast biopsy system. Accessed October 25, 2022. https://www.affirmpronebiopsy.com/
17. Saslow D, Boetes C, Burke W, et al. American cancer society guidelines for breast screening with MRI as an adjunct to mammography. *CA Cancer J Clin*. 2007;57(2):75-89. https://doi.org/10.1097/01.ogx.0000269073.50925.38
18. LaTrenta LR, Menell JH, Morris EA, Abramson AF, Dershaw DDLL, Liberman L. Breast lesions detected with MR imaging: utility and histopathologic importance of identification with US. *Radiology*. 2003;227(3):856-861. https://doi.org/10.1148/radiol.2273012210
19. Yang B, Roys S, Tan U, et al. Design, development, and evaluation of a master – slave surgical system for breast biopsy under continuous MRI. *Int J Rob Res*. 2014;33(4):616-630. https://doi.org/10.1177/0278364913500365
20. Chan KG, Fielding T, Anvari M. An image-guided automated robot for MRI breast biopsy. *Int J Med Robot Comput Assist Surg*. 2016;12(3):461-477. https://doi.org/10.1002/rcs
21. Park SB, Kim J-G, Lim K-W, et al. A magnetic resonance image-guided breast needle intervention robot system: overview and design considerations. *Int J Comput Assist Radiol Surg*. 2017;12(8):1319-1331. https://doi.org/10.1007/s11548-017-1528-2
22. Antoniou A, Drakos T, Giannakou M, et al. Simple methods to test the accuracy of MRgFUS robotic systems. *Int J Med Robot*

Comput Assist Surg. 2021;17(4):e2287. https://doi.org/10.1002/rcs.2287

23. Giannakou M, Yiallouras C, Menikou G, Ioannides C, Damianou C. MRI-guided frameless biopsy robotic system with the inclusion of unfocused ultrasound transducer for brain cancer ablation. *Int J Med Robot Comput Assist Surg*. 2019;15(1):1-9. https://doi.org/10.1002/rcs.1951
24. Patriciu A, Petrisor D, Muntener M, Mazilu D, Schär M, Stoianovici D. Automatic brachytherapy seed placement under MRI guidance. *IEEE Trans Biomed Eng*. 2007;54(8):1499-1506. https://doi.org/10.1109/TBME.2007.900816
25. Patel N, Yan J, Monfaredi R, Sharma K, Cleary K, Iordachita I. Pre-clinical evaluation of an integrated robotic system for magnetic resonance imaging guided shoulder arthrography. *Med Imaging*. 2019;6(2):025006. https://doi.org/10.1117/1.JMI.6.2.025006
26. Dou H, Jiang S, Yang Z, Sun L, Ma X, Huo B. Design and validation of a CT-guided robotic system for lung cancer brachytherapy. *Med Phys*. 2017;44(9):4828-4837. https://doi.org/10.1002/mp.12435
27. Tavallaei MA, Johnson PM, Liu J, Drangova M. Design and evaluation of an MRI-compatible linear motion stage. *Med Phys*. 2016;43(1):62-71. https://doi.org/10.1118/1.4937780
28. Koseki Y, Washio T, Chinzei K, Iseki H. Endoscope manipulator for trans-nasal neurosurgery, optimized for and compatible to vertical field open MRI. In: *Proceedings of the Medical Image Computing and Computer-Assisted Intervention—MICCAI 2002: 5th International Conference Tokyo, Japan, September 25–28*. Vol 2488. Springer; 2002:114-121.
29. *Ultrasound-guided breast biopsy phantom | products: patient simulators for diagnostic training*. Kyotokagaku Co., Ltd. Kyotokagaku.com. Accessed April 30, 2023. https://www.kyotokagaku.com/products/detail01/us-9.html
30. *Stereotactic needle biopsy phantom - CIRS*. CIRS. Accessed April 30, 2023. https://www.cirsinc.com/products/mammography/stereotactic-needle-biopsy-phantom/
31. *Multi-modality breast biopsy and sonographic trainer - CIRS*. CIRS. Accessed April 30, 2023. https://www.cirsinc.com/products/ultrasound/zerdine-hydrogel/multi-modality-breast-biopsy-and-sonographic-trainer/
32. *Sun nuclear breast biopsy Phantoms (GammexTM technology) - sun nuclear*. Sunnuclear.com. Accessed April 30, 2023. https://www.sunnuclear.com/products/breast-biopsy-phantom-s
33. Ng SY, Lin C. Low-cost and easily fabricated ultrasound-guided breast phantom for breast biopsy training. *Res Sci*. 2020:1-22. https://doi.org/10.21203/rs.2.19957/v1
34. Werner R, Krueger S, Winkel A, et al. MR-guided breast biopsy using an active marker: a phantom study. *J Magn Reson Imaging*. 2006;24(1):235-241. https://doi.org/10.1002/jmri.20600
35. Schneider E, Rohling KW, Schnall MD, Giaquinto RO, Morris EA, Ballon D. An apparatus for MR-guided breast lesion localization and core biopsy: design and preliminary results. *J Magn Reson Imaging*. 2001;14(3):243-253. https://doi.org/10.1002/jmri.1180
36. Pfleiderer SOR, Marx C, Vagner J, Franke R-P, Reichenbach JR, Kaiser WA. Magnetic resonance-guided large-core breast biopsy inside a 1.5-T magnetic resonance scanner using an automatic system: in vitro experiments and preliminary clinical experience in four patients. *Invest Radiol*. 2005;40(7):458-463. https://doi.org/10.1097/01.rli.0000167423.27180.54
37. Tang AM, Kacher DF, Lam EY, Wong KK, Jolesz FA, Yang ES. Simultaneous ultrasound and MRI system for breast biopsy: compatibility assessment and demonstration in a dual modality phantom. *IEEE Trans Med Imaging*. 2008;27(2):247-254. https://doi.org/10.1109/TMI.2007.911000
38. Liu W, Yang Z, Feng D, Zhang D. Design and implementation of a new cable-driven robot for MRI-guided breast biopsy. *Int J Med Robot Comput Assist Surg*. 2020;16(2):e2063. https://doi.org/10.1002/rcs.2063
39. Surry KJM, Smith WL, Campbell LJ, Mills GR, Downey DB, Fenster A. The development and evaluation of a three-dimensional ultrasound-guided breast biopsy apparatus. *Med Image Anal*. 2002;6(3):301-312. https://doi.org/10.1016/s1361-8415(02)00087-7
40. Schmidt G, Gerlinger C, Endrikat J, et al. Teaching breast ultrasound skills including core-needle biopsies on a phantom enhances undergraduate student's knowledge and learning satisfaction. *Arch Gynecol Obstet*. 2021;304(1):197-202. https://doi.org/10.1007/s00404-021-06016-8
41. Ng SY, Lin C-L. A multilayered, lesion-embedded ultrasound breast phantom with realistic visual and haptic feedback for needle biopsy. *Ultrasound Med Biol*. 2022;48(8):1468-1483. https://doi.org/10.1016/j.ultrasmedbio.2022.03.009
42. Antoniou A, Damianou C. MR relaxation properties of tissue-mimicking phantoms. *Ultrasonics*. 2022;119:106600. https://doi.org/10.1016/j.ultras.2021.106600
43. Menikou G, Yiannakou M, Yiallouras C, Ioannides C, Damianou C. MRI-compatible bone phantom for evaluating ultrasonic thermal exposures. *Ultrasonics*. 2016;71:12-19. https://doi.org/10.1016/j.ultras.2016.05.020
44. Menikou G, Yiannakou M, Yiallouras C, Ioannides C, Damianou C. MRI-compatible breast/rib phantom for evaluating ultrasonic thermal exposures. *Int J Med Robot Comput Assist Surg*. 2018;14(1):1-12. https://doi.org/10.1002/rcs.1849
45. Drakos T, Giannakou M, Menikou G, Ioannides C, Damianou C. An improved method to estimate ultrasonic absorption in agar-based gel phantom using thermocouples and MR thermometry. *Ultrasonics*. 2020;103:106089. https://doi.org/10.1016/j.ultras.2020.106089
46. Drakos T, Antoniou A, Evripidou N, et al. Ultrasonic attenuation of an agar, silicon dioxide, and evaporated milk gel phantom. *J Med Ultrasound*. 2021;29(4):239-249. https://doi.org/10.4103/JMU.JMU
47. Drakos T, Giannakou M, Menikou G, Constantinides G, Damianou C. Characterization of a soft tissue-mimicking agar/wood powder material for MRgFUS applications. *Ultrasonics*. 2021;113:10635. https://doi.org/10.1016/j.ultras.2021.106357
48. Menikou G, Damianou C. Acoustic and thermal characterization of agar based phantoms used for evaluating focused ultrasound exposures. *J Ther Ultrasound*. 2017;5(1):14. https://doi.org/10.1186/s40349-017-0093-z
49. Antoniou A, Georgiou L, Christodoulou T, et al. MR relaxation times of agar-based tissue-mimicking phantoms. *J Appl Clin Med Phys*. 2022;23(5):213533. https://doi.org/10.1002/acm2.13533
50. Woods TO. Standards for medical devices in MRI: present and future. *J Magn Reson Imaging*. 2007;26(5):1186-1189. https://doi.org/10.1002/jmri.21140
51. Daniel BL, Freeman LJ, Pyzoha JM, et al. An MRI-compatible semi-automated VacuumAssisted breast biopsy system: initial feasibility study. *J Magn Reson Imaging*. 2005;644(5):637-644. https://doi.org/10.1002/jmri.20302
52. Daniel BL, Birdwell RL, Black JW, Ikeda DM, Glover GH, Herfkens RJ. Interactive MR-guided, 14-gauge core-needle biopsy of enhancing lesions in a breast phantom model. *Acad Radiol*. 1997;4(7):508-512. https://doi.org/10.1016/S1076-6332(97)80238-3
53. Drakos T, Giannakou M, Menikou G, Damianou C. Magnetic resonance imaging–guided focused ultrasound positioning system for preclinical studies in small animals. *J Ultrasound Med*. 2020;40(7):1-10. https://doi.org/10.1002/jum.15514
54. Antoniou A, Georgiou L, Evripidou N, Ioannides C, Damianou C. Challenges regarding MR compatibility of an MRgFUS robotic system. *J Magn Reson*. 2022;344:107317. https://doi.org/10.1016/j.jmr.2022.107317

55. Cancer.Net. Breast cancer - stages. Accessed April 15, 2023. https://www.cancer.net/cancer-types/breast-cancer/stages
56. Epaminonda E, Drakos T, Kalogirou C, Theodoulou M, Yiallouras C, Damianou C. MRI guided focused ultrasound robotic system for the treatment of gynaecological tumors. *Int J Med Robot Comput Assist Surg*. 2016;12(1):46-52. https://doi.org/10.1002/rcs.1653
57. Menikou G, Yiallouras C, Yiannakou M, Damianou C. MRI-guided focused ultrasound robotic system for the treatment of bone cancer. *Int J Med Robot Comput Assist Surg*. 2017;13(1):1-11. https://doi.org/10.1002/rcs.1753
58. Hargreaves B, Worters PW, Pauly KB, Pauly JM, Koch KM, Gold GE. Metal induced artifacts in MRI. *Am J Roentgenol*. 2011;197(3):547-555. https://doi.org/10.2214/AJR
59. Mann RM, Kuhl CK, Moy L. Contrast-enhanced MRI for breast cancer screening. *J Magn Reson Imaging*. 2019;50(2):377-390. https://doi.org/10.1002/jmri.26654

How to cite this article: Antoniou A, Nikolaou A, Evripidou N, et al. Phantom-based assessment of motion and needle targeting accuracy of robotic devices for magnetic resonance imaging-guided needle biopsy. *Int J Med Robot*. 2023;e2526. https://doi.org/10.1002/rcs.2526

Scientific paper No.2

Development and evaluation of a robotic device for MRI-guided needle breast biopsy

Cleanthis Ioannides[a], Anastasia Antoniou[b], Vasiliki Zinonos[b], Christakis Damianou[b*]

[a] German Oncology Center, Department of Interventional Radiology, Limassol, Cyprus

[b] Department of Electrical Engineering, Computer Engineering, and Informatics,

Cyprus University of Technology, Limassol, Cyprus.

* For correspondence contact:

Prof. Christakis Damianou,

Department of Electrical Engineering, Computer Engineering, and Informatics,

Cyprus University of Technology,

30 Archbishop Kyprianou Street, 3036 Limassol, Cyprus,

E-mail: christakis.damianou@cut.ac.cy, Tel: 0035725002039, Fax: 0035725002849

MANUSCRIPT TYPE: Original Article

FUNDED BY: Research and Innovation Foundation of Cyprus

WORD COUNT: 7257

FIGURES: 11

ABSTRACT

Background: This study concerns the development and evaluation of a robotic system intended for Magnetic Resonance Imaging (MRI)-guided needle breast biopsy with lateral needle approach.

Methods: The device comprises two piezoelectrically-actuated linear stages intended to aligning a needle supporter with the target location for manual needle insertion by the doctor. Evaluation of targeting accuracy was performed in an in-house agar-based phantom simulating the MR relaxation properties of real tissue in the laboratory and a 3T scanner.

Results: Tumour simulators of 5, 10, and 15 mm diameter were punctured successfully by the needle in 10/10 trials. Accurate placement of a water-filled syringe relative to each target was evidenced by MRI, simultaneously verifying the system's compatibility with a high field scanner.

Conclusions: The developed MRI compatible robotic biopsy device is characterized by a simplified design and advanced ergonomics. Feasibility phantom studies showed high accuracy and repeatability of targeting. The proposed device has potential for future clinical use upon further validation.

KEYWORDS: MRI-guided, breast biopsy, positioning device, agar phantom, accuracy

1. INTRODUCTION

The use of robotically assisted, image-guided percutaneous biopsies over conventional ones that rely on manual insertion of the biopsy needle by the radiologist has grown over time offering less invasiveness and quicker recovery.[1,2] Accordingly, biopsy procedures have become more reliable thanks to the improved stability and accuracy of robotic manipulators compared to human hands. Typically, localization of the suspicious lesion and guidance of the needle manipulator are based on ultrasound (US), magnetic resonance imaging (MRI), and computed tomography (CT) image feedback.[1,2]

Globally, the most prevalent type of cancer malignancy and the sixth leading cause of cancer-related death in women is breast cancer.[3-4] A triple diagnostic method is followed including clinical examination, imaging assessment, and then percutaneous biopsy in case of lesions suspected of malignancy. US is the preferred modality for image-guided biopsy of lesions identifiable on US, where free-handed core biopsy (CB) sampling is typically utilized. It provides real-time guidance without ionizing radiation and accessibility to all breast areas.[5,6] Various robotic systems for US needle guidance have been developed on experimental level through the years[7–12] to facilitate doctors who usually suffer from fatigue and musculoskeletal problems.[13] Most of them are based on the same principle, where the doctor marks the region of interest (ROI) on the relevant US image for registration in the robot's coordinates, which then moves to align the needle with the desired location for final insertion by the doctor.[14]

Around two decades ago, Megali et al.[7] proposed an US-guided biopsy system comprising an already existing robotic arm with eight degrees of freedom (DOF), a 3D optical localizer for tracking the main system's components, and the relevant computer-based main processing unit. Mallapragada et al.[15,16] followed a different approach and developed a robotic system for manipulating the breast mass instead of the needle. Around the same time, a 2D US-guided

two-DOF robotic arm comprising a 14G needle was developed and found to possess a mean trajectory error of 0.75 ± 0.42 mm.[8] The system was tested by radiologists on chicken tissue and found to be faster and more accurate than the free-hand technique.[8] Another robotic system was developed by Smith et. al.[9] for CB under 3D US guidance simultaneously offering breast stabilization. Nelson et al.[10] presented a complete biopsy system comprising a six-DOF robotic arm that was integrated with an US imaging system offering volume breast US data, as well as a dedicated table for prone positioning of the patient. Its targeting accuracy was tested based on a camera tracking technique and found to be within ±1 mm. Notable, a later study[11] introduced a needle steering system that combines a two-DOF needle insertion device with a five-DOF system designed for maneuvering an US transducer to obtain 3D imaging data.[11] More recently, a mechanical end-effector for robotically-assisted 3D US breast scanning and biopsy that can accommodate needles of any size has been proposed.[12] This system enables needle guidance in three DOF while needle insertion is performed by the user.

Lesions that are not identifiable on US images are typically sampled under stereotactic mammography guidance.[17] This procedure can be performed either on a dedicated biopsy table with the patient in the prone position, or by fixing an add-on stereotactic unit on the existing mammographic equipment.[18] In both techniques, the breast is compressed and vacuum assisted biopsy (VAB) sampling is usually preferred due to the smaller rates of false-negative results.[19] There are several marketed robotic systems for automatic needle alignment. As an example, the Affirm biopsy system exists both as an add-on unit[20] and a table system,[21] offering needle guidance in the cartesian coordinate system, as well as 2D and tomosynthesis imaging capabilities. They are both based on mammographic images, on which the doctor marks the ROI. The needle holder is automatically moved to the corresponding coordinates in the X-Y plane with an estimated targeting accuracy of 1 mm for manual insertion of the needle in the Z direction. Interestingly, a few mechanical systems have been developed on a research level

combining both US and stereotactic mammography guidance to overcome the limitations each modality presents when used as a stand-alone method.[22–24]

MRI is considered a superior guidance modality in that it can detect lesions while still being occult in traditional examinations and it is recommended especially for women being at high risk of developing breast cancer.[25,26] In such cases, an MR-guided biopsy is needed to histologically determine possible malignancy of the tumour. The patient is commonly in a prone position on a specially designed MR bed with a hole for the breasts, which are immobilized by vertical compression plates for avoiding any shift during the procedure.[27] An initial scanning is conducted for lesion localization. The optimum hole of a localization grid (lying in line with the lesion), as well as the insertion depth of the needle are determined by a combined biopsy software.[27] The patient is then moved out of the bore and a sheath is inserted, through which the biopsy needle will be advanced to the target. The coaxial sheath is placed with the help of a stylet, which is replaced by a plastic MRI-visible obturator. An additional scan is followed to confirm that the obturator's location coincides with that of the target.[27] The biopsy is usually performed outside of the magnet and involves inserting a hollow needle towards the lesion. Lateral approach of the needle is recommended,[28] especially for deep lesions,[29] with the localization methods involving grid, pillar and post, as well as free-hands techniques.[30]

Even though high successful rates of the current approach of MR-guided breast biopsy have been achieved in several studies, the technique has a number of drawbacks, such as the necessity of repetitively moving the patient into and out of the scanner, the possible lesion movement due to involuntary movements or tissue-needle interaction, the acquisition of large volumes of tissue and the prolonged procedures.[31] Therefore, a robotic contribution is required

for addressing the aforesaid limitations, thus providing a more accurate and efficient biopsy of the involved lesions.

Some initial trials for robotic breast interventions in the MRI setting resulted in the development of a six-DOF robotic system for both biopsy and therapy of breast tumours,[32] a system featuring five DOF for minimally-invasive remote intervention in the breast by means of ultrasonic motors,[33] and a single-DOF teleoperated needle driver robot.[34] Later, a six-DOF master-slave robotic system intended to be placed underneath the headrest was developed[35] for accurate needle positioning and insertion. Actuated by five pneumatic cylinders and one piezomotor, the slave robot can be tracked in the MRI coordinates allowing the physician to operate the master console under real-time MRI guidance. Although sufficient target accuracy of a 12G MRI coaxial needle was achieved, the robot workspace is confined and access to challenging lesion locations is infeasible.[35] A six-DOF image-guided automated robot (IGAR) actuated by piezoelectric motors was also designed to be accommodated under the headrest.[36] Needle interventions were performed only outside of the MRI bore utilizing an introducer-localization system demonstrating a sub-millimeter targeting ability in free space.[36]

More recently, a piezoelectrically actuated robotic manipulation system (MR-SON) with four DOF controlled by an image guidance software was manufactured.[37] Its slim design makes it suitable for lateral approach of the needle since it can fit in the MRI bore between the patient and the gantry. Due to the confined workspace, the system features a bendable 13-G needle. Experiments performed in a breast phantom showed a targeting accuracy of ± 2.5 mm. Although the lateral approach is considered advantageous for targeting challenging lesions, insertion of the bendable needle is limited only in several directions.[37]

More technological advances have seen the production of the “Stormram 4”, which is a four-DOF serial kinematic manipulator driven by two liner and two curved pneumatic stepper

motors.[38] It constitutes a 3D-printed improved version of earlier designs,[39,40] in terms of accuracy, size, complexity, and available workspace. It utilizes curved air-pressure motors allowing it to fit and operate inside the MRI scanner. Lateral approaches for automatic insertion of the needle are allowed. According to trials in breast phantoms, this robot offers needle targeting with a mean positioning error of 1.29 ± 0.59 mm.

It is interesting that a novel palm-shaped breast deformation robot was designed[41] to be placed in the MR bore with the aim to optimize breast compression and provide flexible breast configuration and comfort to the patients. With multiple-DOF actuated by a piezoelectric motor and multiple pneumatic bladders, the robot can compress the breast in multiple angles, thus increasing the biopsy precision.[41]

In this study, we propose an MRI-compatible breast biopsy robotic device that is characterized by a simplified design with all the mechanical components being arranged in a slim rectangular enclosure that is placed laterally to the patient. The device comprises two 3D-printed piezoelectrically-actuated linear stages of motion that are based on jackscrew mechanisms for positioning a needle supporter along the anterior-posterior and inferior-superior axes of an MRI scanner. Remote control of the mechanism is achieved through an electronic driving system, which is in turn interfaced with a custom-made biopsy planning software.

The device proposed herein is universal since it can be seated on the table of any conventional scanner of up to 7T while previous devices are positioned underneath the patient,[35,36] thus requiring modification of the MRI table or the addition of a dedicated one. It is also easily portable due to its small size and light weight, as well as straightforward and ergonomic to use through the user-friendly commands of the biopsy software. In contrast with existing devices,[37–39] the system is also considered to offer advanced safety features since there are no

moving parts in the scanner. Furthermore, manual insertion of the needle by the physician does not withdraw the factor of “human control”.

The performance of the developed biopsy system in terms of accurate and repeatable needle targeting was assessed by laboratory and MRI studies in a dedicated agar-based phantom with tumour simulators, which was designed to mimic critical MRI properties of real tissue. Notably, tissue mimicking phantoms based on agar have become a key tool in the preclinical testing of medical systems and protocols.[42–46]

2. MATERIALS AND METHODS

2.1 Robotic design

The robotic device was specially designed on the Inventor Software® (Autodesk, San Rafael, California, United States) to operate in the MRI scanner for needle breast biopsy through a lateral approach and manufactured on a rabid prototyping system (FDM400, Stratasys, 7665 Commerce Way, Eden Prairie, Minnesota, 55344, USA) using Acrylonitrile styrene acrylate (ASA) and Polylactic acid (PLA) thermoplastics. It comprises a positioning mechanism intended to navigating a biopsy needle to align with a target position. The mechanism consists of two piezoelectrically-actuated (USR60-S3N, Shinsei Kogyo Corp., Tokyo, Japan) motion stages offering linear motion in two orthogonal axes (X and Y). Optical encoders (EM1-0-500-I, US Digital Corporation, Vancouver, Washington, USA) were incorporated to provide motion feedback, thus ensuring accurate needle positioning.

The Y-stage enables adjusting the needle’s position in the vertical axis extending in anterior-posterior direction with the use of a jackscrew mechanism. As shown in the Computer Aided Design (CAD) drawing of Figure 1a, the Y-axis jackscrew has a first end attached to the Y-axis motor while being advanced through the respective threaded hole of the Y-axis driver

brace so as to convert the angular motion of the motor into linear motion of the brace. Two plastic drive shafts were incorporated enhancing motion stability of the driver brace. As it can also be seen in Figure 1a, the driver brace includes three equally spaced holes that can accommodate a needle supporter, thus increasing the available motion range.

The X-stage shown in Figure 1b enables adjustment of the needle's position in the horizontal axis, which extends in superior-inferior direction. Motion of the X-stage is actuated based on the same principle as the Y-stage but through a quite more complicated mechanism. Specifically, the angular motion of the X-axis motor is transmitted vertically to two jackscrews located at the top and bottom opposite sides of the stage through a series of gears. Similar to the Y-stage, these jackscrews are advanced though the respective threaded holes of the X-axis drive braces thus converting the angular motion of the motor into simultaneous linear motion of the two braces. Again, a drive shaft was added at each side for enhancing structural stability.

Both stages incorporate an optical encoder system for motion feedback and accurate positioning along the two linear axes. The encoder strips were securely attached to the mechanism extending in the X- and Y-axes with the assistance of dedicated strip holders while the encoder modules were mounted on the respective driver braces, thus moving along the respective stripes for generating position signals during motion. The motion range is 90 and 130 mm in the X- and Y-axes, respectively.

The X- and Y-stages were assembled together and arranged within a rectangular frame as shown in Figure 2a. The CAD drawing of the final device including covers and the needle supporter is shown in Figure 2b whereas Figure 2C is a photo of the manufactured device. In the real environment, the device is intended to be placed between the subject and the MRI bore, as illustrated in Figure 3, thus allowing for lateral needle approach to the breasts.

2.2 Navigation software for MRI-guided needle biopsy

The robot was interfaced with an in-house developed navigation software that includes tools for MRI interfacing, biopsy planning and control of the motion stages. The navigation features enable selection of the target location on pre-operative MR images of the ROI and automatic placement of the needle supporter based on the extracted motion vectors that are sent by the software to the electronic driving system. Remote device control is possible through the software commands and corresponding driving electronics, thereby creating an efficient procedural workflow. The software interface and main navigation tools are shown in Figure 4.

2.3 System's evaluation in MRI compatible phantom

2.3.1 MR relaxation properties of candidate agar-based mixtures

Agar-based phantoms with different concentrations of inclusions were prepared and contained in the rectangular mold shown in Figure 5a, along with two reference liquids (water, oil). Agarose (Merck KGaA, EMD Millipore Corporation, Darmstadt, Germany) and silicon dioxide (Sigma-Aldrich, St. Louis, Missouri, United States) were utilized in different concentrations to demonstrate their effect on MRI properties. Three phantoms were prepared with varying concentration of agarose of 2 – 6 % weight per volume (w/v), which serves as the gelling agent. Various amounts of silicon dioxide (2– 8 % w/v) were added in phantoms with a fixed concentration of 6 % w/v agar. A detailed description of the preparation process can be found in a study by Drakos et al.[47]

The container was sited on the table of a 3T MRI scanner (MAGNETOM Vida, Siemens Healthineers, Erlangen, Germany) for imaging and the Biomatrix 12 channel body coil (Siemens Healthineers) was securely positioned at sufficient distance above the container using a supporting structure. The experimental setup can be seen in Figure 5b.

2.3.1.1 Variable Flip Angle T1 Mapping

Images of the phantoms were obtained in coronal plane using a Gradient Echo (GRE) sequence at variable flip angle (FA) of 5 - 26º for T1 mapping. The data were fitted into the following equation 1:[48]

$$\mathrm{M_z} = \mathrm{M_{0z}}\left(\frac{1-\mathrm{e}^{-\frac{\mathrm{TR}}{\mathrm{T1}}}}{1-\cos a\ \mathrm{e}^{-\frac{\mathrm{TR}}{\mathrm{T1}}}}\right)\sin a \qquad [1]$$

where $\mathrm{M_z}$ is the longitudinal magnetization, $\mathrm{M_{0z}}$ is the magnetization at thermal equilibrium, TR is the pulse sequence repetition time, and a is the excitation flip angle. Image acquisition was performed using the following parameters: repetition time (TR) = 15 ms, echo time (TE) = 1.95 ms, echo train length (ETL) = 1, pixel bandwidth (pBW) = 277 kHz, matrix size = 160 x 160, slice thickness = 5 mm, and number of excitations (NEX) = 1.

2.3.1.2 Variable Echo Time T2 Mapping

A T2-weighted (T2-W) Spin Echo (SE) sequence was employed for estimating the transverse relaxation time. Multiple scans were obtained at variable TE values of 13.8 - 69 ms and the measured signal intensity over TE was fitted to the exponential decay function of equation 2:[49]

$$M_{xy} = M_{xy0}e^{-\frac{TE}{T2}} \qquad [2]$$

where M_{xy} is the transverse magnetization and M_{xy0} is its maximum value. The images were acquired with the following parameters: TR = 1910 ms, TE = 13.8 – 69 ms, FA = 180º, ETL = 5, pBW = 228 kHz, matrix size = 160 x 160, slice thickness = 3 mm, and NEX = 1.

The MR relaxation times of each phantom were estimated through a voxel-by-voxel analysis, where parametric maps were derived from the series of acquired images by fitting the mathematic models to the acquired data for each individual voxel through automated algorithmic processing.

2.3.2 Agar-based phantom development

A phantom containing multiple biopsy targets was then created. The selection of materials' concentration was mainly based on the T1 and T2 measurements of the various agar-silica mixtures and the resultant gel stiffness. Specifically, three cylindrical tumour simulators with diameters of 5, 10, and 15 mm were created my molding in a dedicated 3D-prtined mold. Two gel mixtures of different agar/silica concentration that presented notable difference in both T1 and T2 were utilized for simulating the tumour and breast tissue. The developed phantom was imaged utilizing a T2-W Turbo Spin Echo (TSE) sequence (TR = 2500 ms, TE = 46 ms, FA = 180°, ETL = 8, pBW = 50 Hz/pixel, FOV = 200 x 200 mm^2, matrix size = 128 x 128, slice thickness = 8 mm, and NEX = 1) to evaluate MRI visibility.

2.3.3 Benchtop and MRI targeting accuracy

Evaluation of the accuracy and precision of the needle supporter in reaching biopsy targets was carried out in benchtop and MRI settings. For the purpose of this experiment, a 3-mm plastic needle was 3D-printed using ASA thermoplastic and attached to the needle supporter. The experimental set-up as arranged in the laboratory is illustrated in the photo of Figure 6. The device was connected to the laptop integrating the relevant biopsy software through the custom-made electronic driving system. The agar phantom was fixed within the workspace of the robot on a dedicated holder allowing for direct access to the biopsy targets by the needle.

The needle was repetitively commanded (n=10) to reach each one of the tumour simulators. Guidance of the needle supporter in relation to the target location was planned on previously obtained MR images involving the use of a water filled syringe. The user chose the tumour simulator to be targeted on the relevant phantom image, and then pushed the needle to puncture the phantom following motion execution. The targeting procedure was considered successful when the needle tip was visually detected at the desired position within the tumour simulator.

The experimental set-up for MRI evaluation in the 3T scanner (Magnetom Vida) is presented in Figure 7. The electronic driving system remained outside of the MRI room while being connected to the device through shielded cables. A water-filled syringe was attached to the needle supporter of the robotic device and the phantom was covered by a multichannel body coil (18-channel, Siemens Healthineers). Registration of the needle supporter in relation to the phantom was achieved by acquiring axial scans showing the syringe and phantom. The syringe was then robotically moved from its initial position to align with the target location following navigation planning on T1-Weighted (T1-W) TSE axial images of the relevant ROIs. The following imaging parameters were employed: TR = 700 ms, TE = 22 ms, FOV = 20×20 mm^2, Matrix size = 128×128, ETL = 3, FA = 180^o, Slice thickness = 8 mm, and NEX = 2. Following execution of the commanded motion steps, image acquisition was repeated to assess the accuracy of syringe placement.

3 RESULTS

3.1 MR relaxation properties of candidate agar-based mixtures

Indicative T2-W SE images of the various agar/silica mixtures acquired at different TE values for T2 mapping are presented in Figure 8. Table 1 lists the mean value of the T1 and T2 relaxation times and the corresponding standard deviation of each recipe as estimated by the voxel-by-voxel analysis. Note that both T1 and T2 were gradually decreased with increasing agar concentration (2-6 % w/v). The same behavior is observed with increasing silica concentration (2-8 % w/v).

3.2 Agar-based phantom development

The silica concentration of 8 % w/v (in a 6 % w/v agar gel) resulted in a very stiff phantom, whereas the agar concentration of 2 % w/v (pure agar gel) resulted in a slightly loose phantom, and therefore, the specific recipes were abandoned. Based on the T1 and T2 estimates of the

remaining recipes (Table 1), tumour simulators of 5, 10, and 15 mm diameter were made out of 6 % w/v agar and 4 % w/v silica powder, whereas in the surrounding tissue a 4 % w/v agar and no silica were used. A photo and a T2-W TSE image of the developed phantom are respectively shown in Figures 9a and 9b.

3.3 Benchtop and MRI targeting accuracy

Regarding laboratory evaluation, all three tumour simulators were successfully punctured by the needle in 10/10 trials with high repeatability among repetitions. Successful alignment of the syringe with the targets was also observed in the MRI study. Indicative results of the robot's targeting accuracy are presented in Figures 10 and 11. Figure 10a shows the target location as defined in the software, whereas Figure 10b is an indicative photo of the punctured phantom taken in the laboratory. Note that the needle tip is located at the center of the 5-mm target. Accordingly, Figures 10c and 10d show fused T1-W TSE axial images showing the initial and final (following navigation) location of the syringe in relation to the 5-mm tumour simulator, respectively. The corresponding results obtained for the 10-mm tumour simulator are shown in Figure 11.

4 DISCUSSION

Biopsy procedures have become more reliable thanks to the accuracy and precision of robotically assisted, image-guided percutaneous biopsies. The current study provides a detailed description of a new developed 2-DOF MRI compatible breast biopsy robotic device that was designed to be placed in the MRI scanner laterally to the patient based on the team's vast experience in the design of MRI-guided robotics.[50–56] Both linear stages are actuated by piezoelectric motors and possess an accuracy of about 0.1 mm as estimated through numerous experiments performed to evaluate previous robotic devices of the team, which use the same principle of motion.[57–59] Sufficient evidence of MRI compatibility is also available in previous

publications of the group. Specifically, the device employs materials that were proven proper for integration in the MRI bore in terms of having no significant interaction with the scanner and introducing acceptable noise level when using proper imaging sequences.[55,57–60] It is noted that the use of piezoelectric motors and encoders makes the system MR-conditional in accordance with the F2503 standard of the American Society for Testing and Materials (ASTM) as described by Stoianovici et al.[61]

The manufactured robotic device has a simple, slim and lightweight design that makes it easily transportable, cost-effective and more ergonomic compared to more complex systems having their components moving in the bore of the scanner.[35,37,38] It can be placed between the patient and the gantry allowing for lateral approach of the needle, which is beneficial especially for deep lesions while leaving sufficient space for comfortable placement of the patient.[28] This configuration also enhances the safety of the procedure since there are no moving (mechatronic) parts at the side of the patient. By using this simplified design and the rapid prototyping method, manufacturing and maintenance costs are low as well.

The mechanism comprises the X- and Y-stages of motion that individually move the needle supporter along the X- and Y-axes, respectively, offering a workspace of 90 x 130 mm^2. The jackscrew mechanisms used to generate the linear motion increase the torque of the motors producing a smooth, controllable movement. Furthermore, the motion mechanism possesses high structural stiffness and rigidity that were further increased with the incorporation of the plastic shafts, thereby offering stable positioning of the water-filled syringe or needle, as well as the load capacity to accommodate a biopsy gun in future experiments. Placement of the needle supporter relative to the target is achieved remotely through a custom-developed biopsy software that was interfaced with the robotic device allowing for needle navigation planning on MR images of the ROIs and real-time monitoring of motion execution through its interface.

The creation of a phantom with three targets of varying diameter was the initial stage of the assessment process. The phantom was designed to evaluate the preclinical effectiveness of the developed biopsy system in terms of the accuracy of needle placement in laboratory and MRI environments. T1 and T2 measurements of different mixtures of agar and silicon dioxide powders were initially conducted to investigate the effect of varying the concentration of these ingredients on the resultant relaxation times. Both T1 and T2 were gradually decreased with increasing amount of agar and silica. A similar trend was observed in a previous study,[62] in which T1 and T2 mapping was performed in a 1.5 T MRI scanner. Herein, the estimated T2 relaxation times ranged from 23 to 112 ms (3T) and are partly consistent with the values reported for soft tissues in a review article by Bottomley et al.[63] roughly ranging from 40 to 80 ms. Note that the T2 value of oil could not be measured because of chemical shift artifacts that were obscuring the location of the measurement. Regarding the longitudinal relaxation time T1, literature values (at 3 T) are harshly between 500 and 1000 ms[64] for soft tissues and between 898 and 1509 ms for muscle.[49] The T1 estimates (3T) for the agar-based phantoms are higher, ranging from 1975 to 3080 ms.

The variation of properties among the tested recipes allowed the creation of tumour simulators with excellent MRI visibility. In fact, the mixture containing 6 % w/v agar and 4 % w/v silica powder and the one containing only 4 % w/v agar that showed sufficient difference in their MR relaxation times were selected to mimic tumour and breast tissue, respectively. SE imaging yielded phantom images of very good quality in terms of contrast and resolution with very good delineation of the phantom edges and all biopsy targets.

In this study, evaluation of the system's performance was focused on the accuracy and repeatability of targeting biopsy targets embedded in a gel phantom. All three tumour simulators were sequentially targeted in laboratory and MRI studies. In each case, the two

dimensional path of the needle supporter was extracted from the software based on the obtained axial images illustrating the syringe and the phantom at the level of the tumour simulators.

In the benchtop study, a plastic needle made out of ASA was attached to the robot and repetitively commanded to align with each tumour mimic for final insertion by the user (n=10). The results showed excellent targeting repeatability with no off-target insertions (Figures 10b and 11b). Similarly, MRI evaluation involved navigating a water-filled syringe as attached to the needle supporter to align with the target's position, where the positioning accuracy was examined by fusing MRI scans of the syringe and target. In all cases, the syringe was observed as a white spot at the desired location within the tumour simulator, which appeared with reduced intensity compared to the surrounding breast mimicking material (Figures 10d and 11d). These findings further demonstrate the software's functionality, and that the system responds properly in the real environment in terms of executing the software's commands correctly and maintaining accurate needle placement without compromising the quality of imaging.

5 CONCLUSIONS

The study introduced an MRI compatible robotic biopsy device that is characterized by a simplified design and advanced ergonomics. Phantom studies provide initial evidence of accurate targeting in both the laboratory and MRI room, as well as proper software functionality and communication with the relevant hardware. Overall, the system possesses potential for future clinical use upon further evaluation of the accuracy and repeatability in the real environment. In this regard, the system may be equipped with a breast stabilization system and a biopsy gun for the acquisition of tissue samples.

ACKNOWLEDGMENTS

The project MRBREASTBIO (CONCEPT/0521/0040) is implemented under the programme of social cohesion “THALIA 2021-2027” co-funded by the European Union, through Research and Innovation Foundation.

CONFLICT OF INTERESTS

Authors declare no conflict of interest.

PRIOR OR DUBLICATE PUBLICATION

Not applicable.

ETHICS APPROVAL DECLARATION

The study does not include data on patients or animals. No ethical approval is available.

Phantom #	Material Composition	T1 ± SD (ms)	T2 ± SD (ms)
1	2 % agar	3080.1 ± 121	111.7 ± 2.6
2	4 % agar	2486.2 ± 53.9	53.3 ± 1.5
3	6 % agar	2137.9 ± 30.5	40.2 ± 2.2
4	6 % agar, 2% silica	2259.6 ± 41.2	32.9 ± 0.8
5	6 % agar, 4% silica	2040.7 ± 47	29.7 ± 0.7
6	6 % agar, 6% silica	2039.2 ± 38.4	23.8 ± 0.6
7	6 % agar, 8% silica	1975 ± 54.2	22.7 ± 0.7
8	Water	3468.9 ± 238.6	96.4 ± 2
9	oil	309.8 ± 4.3	-

Table 1: Mean values of T1 and T2 relaxation times and the corresponding standard deviation (SD) of each phantom recipe as estimated by voxel-based analysis.

LIST OF FIGURES LEGENDS

Figure 1: CAD drawings of the (a) X-stage and (b) Y-stage indicating the various components**.**

Figure 2: CAD drawings of the (a) assembled mechanism integrated within the frame and (b) final device with all mechanical parts enclosed within the outer cover. (c) Photo of the manufactured device.

Figure 3: CAD drawing of the biopsy device placed in the MRI scanner for lateral needle approach to the breast.

Figure 4: Software interface screenshot with the main navigation tools indicated: 1. placing navigation points, 2. controlling motion manually, 3. starting navigation planning, 4. erasing navigation points, 5. "homing" menu, and 6. creating new layers.

Figure 5: (a) Photo of the phantoms in the mold and the corresponding recipe. (b) The experimental setup for T1 and T2 measurements.

Figure 6: Experimental set-up for accuracy evaluation arranged in the laboratory setting with the various system components indicated.

Figure 7: Experimental set-up for accuracy evaluation inside the 3 T MRI scanner with the various system components indicated.

Figure 8: Coronal slices of the phantoms acquired using a T2-W SE sequence at TE values of (A) 13.8, (B) 41.4, and (C) 69 ms. Imaging parameters: TR = 1910 ms, FA = 180º, ETL = 5, pBW = 228 kHz, matrix size = 160 x 160, slice thickness = 3 mm, and NEX = 1.

Figure 9: The developed agar-based biopsy phantom: (a) photo indicating the diameter of each tumour simulator and (b) T2-W TSE coronal image with TR = 2500 ms, TE = 46 ms, FA =

180°, ETL = 8, NEX = 1, pBW = 50 Hz/pixel, FOV = 200 x 200 mm^2, matrix size = 128 x 128, and slice thickness = 8 mm.

Figure 10: (a) Target location set at the 5-mm tumour (red bullet) in the biopsy software. (b) Needle tip location after manual needle insertion in the 5-mm tumour mimic in the laboratory. (c) Fused MR image showing the initial location of the syringe relative to the phantom. (d) Fused MR image showing the syringe within the targeted tumour after navigation. MR images were acquired with a T1-W TSE sequence (TR = 700 ms, TE = 22 ms, FOV = 20×20 mm^2, Slice thickness = 8 mm, ETL = 3, FA = 180^o, Matrix size = 128×128, and NEX = 2).

Figure 11: (a) Target location set at the 10-mm tumour (red bullet) in the biopsy software. (b) Needle tip location after manual needle insertion in the 10-mm tumour mimic in the laboratory. (c) Fused MR image showing the initial location of the syringe relative to the phantom. (d) Fused MR image showing the syringe within the targeted tumour after navigation. MR images were acquired with a T1-W TSE sequence (TR = 700 ms, TE = 22 ms, FOV = 20×20 mm^2, Slice thickness = 8 mm, ETL = 3, FA = 180^o, Matrix size = 128×128, and NEX = 2).

REFERENCES

1. Siepel FJ, Maris B, Welleweerd MK, Groenhuis V, Fiorini P, Stramigioli S. Needle and Biopsy Robots: a Review. *Curr Robot Rep*. 2021;2:73-84. doi:10.1007/s43154-020-00042-1

2. Unger M, Berger J, Melzer A. Robot-Assisted Image-Guided Interventions. *Front Robot AI*. 2021;8:1-7. doi:10.3389/frobt.2021.664622

3. World Health Organization (WHO). Breast Cancer. Source: Globocan 2020. https://gco.iarc.fr/today/data/factsheets/cancers/20-Breast-fact-sheet.pdf. Accessed October 11, 2022.

4. Momenimovahed Z, Salehiniya H. Epidemiological characteristics of and risk factors for breast cancer in the world. *Breast Cancer Targets Ther*. 2019;11:151-164. doi:10.2147/BCTT.S176070

5. Helbich TH, Matzek W, Fuchsjäger MH. Stereotactic and ultrasound-guided breast biopsy. *Eur Radiol*. 2004;14(3):383-393. doi:10.1007/s00330-003-2141-z

6. Schueller G, Schueller-Weidekamm C, Helbich TH. Accuracy of ultrasound-guided, large-core needle breast biopsy. *Eur Radiol*. 2008;18(9):1761-1773. doi:10.1007/s00330-008-0955-4

7. Megali G, Tonet O, Stefanini C, et al. A computer-assisted robotic ultrasound-guided biopsy system for video-assisted surgery. *Lect Notes Comput Sci (including Subser Lect Notes Artif Intell Lect Notes Bioinformatics)*. 2001;2208:343-350. doi:10.1007/3-540-45468-3_41

8. Bluvol N, Sheikh A, Kornecki A, Del Rey Fernandez D, Downey D, Fenster A. A needle

guidance system for biopsy and therapy using two-dimensional ultrasound. *Med Phys*. 2008;35(2):617-628. doi:10.1118/1.2829871

9. Smith WL, Surry KJM, Mills GR, Downey DB, Fenster A. Three-Dimensional Ultrasound-Guided Core Needle Breast Biopsy. *Ultrasound Med Biol*. 2001;27(8):1025-1034.

10. Nelson TR, Tran A, Fakourfar H, Nebeker J. Positional calibration of an ultrasound image-guided robotic breast biopsy system. *J Ultrasound Med*. 2012;31(3):351-359. doi:10.7863/jum.2012.31.3.351

11. Abayazid M, Moreira P, Shahriari N, Patil S, Alterovitz R, Misra S. Ultrasound-guided three-dimensional needle steering in biological tissue with curved surfaces. *Med Eng Phys*. 2015;37(1):145-150. doi:10.1016/j.medengphy.2014.10.005

12. Welleweerd MK, Siepel FJ, Groenhuis V, Veltman J, Stramigioli S. Design of an end-effector for robot-assisted ultrasound-guided breast biopsies. *Int J Comput Assist Radiol Surg*. 2020;15(4):681-690. doi:10.1007/s11548-020-02122-1

13. Sommerich CM, Lavender SA, Evans K, et al. Collaborating with cardiac sonographers to develop work-related musculoskeletal disorder interventions. *Ergonomics*. 2016;59(9):1193-1204. doi:10.1080/00140139.2015.1116613.

14. Priester AM, Natarajan S, Culjat M. Robotic ultrasound systems in medicine. *IEEE Trans Ultrason Ferroelectr Freq Control*. 2013;60(3):507-523. doi:10.1109/TUFFC.2013.2593

15. Mallapragada VG, Sarkar N, Podder TK. Robot-assisted real-time tumor manipulation for breast biopsy. *IEEE Trans Robot*. 2009;25(2):316-324.

doi:10.1109/TRO.2008.2011418

16. Mallapragada V, Sarkar N, Podder TK. Toward a robot-assisted breast intervention system. *IEEE/ASME Trans Mechatronics*. 2011;16(6):1011-1020. doi:10.1109/TMECH.2010.2068575

17. Ames V, Britton PD. Stereotactically guided breast biopsy: a review. *Insights Imaging*. 2011;2(2):171-176. doi:10.1007/s13244-010-0064-1

18. Michell M. *Breast Cancer*. 1st ed. Cambridge University Press; 2010. doi:10.1017/CBO9781107415324.004

19. Patterson SK. Image-guided percutaneous breast biopsies. *Imaging Med*. 2011;3(5):597-605. doi:10.2217/iim.11.42

20. Hologic. Affirm Breast Biopsy Guidance System. https://www.hologic.com/hologic-products/breast-health-solutions/affirm-breast-biopsy-guidance-system. Accessed October 25, 2022.

21. Hologic. Affirm Prone Breast Biopsy System. https://www.affirmpronebiopsy.com/. Accessed October 25, 2022.

22. Surry KJM, Mills GR, Bevan K, Downey DB, Fenster A. Stereotactic mammography imaging combined with 3D US imaging for image guided breast biopsy. *Med Phys*. 2007;34(11):4348-4358. doi:10.1118/1.2794175

23. Surry KJM, Smith WL, Campbell LJ, Mills GR, Downey DB, Fenster A. The development and evaluation of a three-dimensional ultrasound-guided breast biopsy apparatus. *Med Image Anal*. 2002;6:301-312.

24. Fenster A, Surry KJM, Mills GR, Downney DB. 3D ultrasound guided breast biopsy

system. *Ultrasonics*. 2004;42:769-774. doi:10.1016/j.ultras.2003.11.004

25. Saslow D, Boetes C, Burke W, et al. American Cancer Society Guidelines for Breast Screening with MRI as an Adjunct to Mammography. *CA Cancer J Clin*. 2007;57(2):75-89.

26. Gao P, Kong X, Song Y, et al. Recent progress for the techniques of MRI-guided breast interventions and their applications on surgical strategy. *J Cancer*. 2020;11(16):4671-4682. doi:10.7150/jca.46329

27. Plantade R, Thomassin-Naggara I. MRI vacuum-assisted breast biopsies. *Diagn Interv Imaging*. 2014;95(9):779-801. doi:10.1016/j.diii.2013.12.023

28. Khouli RH El, Macura KJ, Barker PB, et al. MRI-Guided Vacuum-Assisted Breast Biopsy : A Phantom and Patient Evaluation of Targeting Accuracy. *J Magn Reson Imaging*. 2009;429:424-429. doi:10.1002/jmri.21831

29. Heywang-Köbrunner SH, Sinnatamby R, Lebeau A, Lebrecht A, Britton PD, Schreer I. Interdisciplinary consensus on the uses and technique of MR-guided vacuum-assisted breast biopsy (VAB): Results of a European consensus meeting. *Eur J Radiol*. 2009;72(2):289-294. doi:10.1016/j.ejrad.2008.07.010

30. Gombos EC, Hospital W, Jagadeesan J, et al. MR guided breast interventions: role in biopsy targeting and lumpectomies. *Magn Reson Imaging Clin N Am*. 2016;23(4):547-561. doi:10.1016/j.mric.2015.05.004.MR

31. Chevrier MC, David J, Khoury M El, Lalonde L, Labelle M, Trop I. Breast Biopsies Under Magnetic Resonance Imaging Guidance: Challenges of an Essential but Imperfect Technique. *Curr Probl Diagn Radiol*. 2016;45(3):193-204.

doi:10.1067/j.cpradiol.2015.07.002

32. Kaiser W, Fischer H, Vagner J, Selig M. Robotic System for Biopsy and Therapy of Breast Lesions in a High-Field Whole-Body Magnetic Resonance Tomography Unit. *Invest Radiol*. 2000;35(8):513-519.

33. Larson BT, Erdman AG, Tsekos N V., Yacoub E, Tsekos P V., Koutlas IG. Design of an MRI-Compatible Robotic Stereotactic Device for Minimally Invasive Interventions in the Breast. *J Biomech Eng*. 2004;126(4):458-465.

34. Kokes R, Lister K, Gullapalli R, et al. Towards a Teleoperated Needle Driver Robot with Haptic Feedback for RFA of Breast Tumors under Continuous MRI. *Med Image Anal*. 2009;13(3):445-455. doi:10.1016/j.media.2009.02.001

35. Yang B, Roys S, Tan U, et al. Design , development , and evaluation of a master – slave surgical system for breast biopsy under continuous MRI. *Int J Rob Res*. 2014;33(4):616-630. doi:10.1177/0278364913500365

36. Chan KG, Fielding T, Anvari M. An image-guided automated robot for MRI breast biopsy. *Int J Med Robot Comput Assist Surg*. 2016;12(3):461-477. doi:10.1002/rcs

37. Park SB, Kim J-G, Lim K-W, et al. A magnetic resonance image-guided breast needle intervention robot system : overview and design considerations. *Int J Comput Assist Radiol Surg*. 2017;12(8):1319-1331. doi:10.1007/s11548-017-1528-2

38. Groenhuis V, Siepel FJ, Veltman J, van Zandwijk JK, Stramigioli S. Stormram 4: An MR Safe Robotic System for Breast Biopsy. *Ann Biomed Eng*. 2018;46(10):1686-1696. doi:10.1007/s10439-018-2051-5

39. Groenhuis V, Veltman J, Stramigioli S. Stormram 2: A MRI-compatible robotic system

for breast biopsy. In: *Proceedings of The Hamlyn Symposium on Medical Robotics*. Imperial College; 2016:52-53.

40. Groenhuis V, Veltman J, Siepel J, Stramigioli S. Stormram 3: A Magnetic Resonance Imaging-Compatible Robotic System for Breast Biopsy. In: *Special Issue on Surgical Robot Challenge*. IEEE; 2017:34-41.

41. Zhang T, Navarro-alarcon D, Ng KW, Chow MK, Liu Y, Chung HL. A Novel Palm-Shape Breast Deformation Robot for MRI-Guided Biopsy A Novel Palm-Shape Breast Deformation Robot for MRI-Guided Biopsy. In: *2016 IEEE International Conference on Robotics and Biomimetics (ROBIO)*. ; 2016:527-532. doi:10.1109/ROBIO.2016.7866376

42. Menikou G, Damianou C. Acoustic and thermal characterization of agar based phantoms used for evaluating focused ultrasound exposures. *J Ther Ultrasound*. 2017;5. doi:10.1186/s40349-017-0093-z

43. Drakos T, Antoniou A, Evripidou N, et al. Ultrasonic Attenuation of an Agar, Silicon Dioxide, and Evaporated Milk Gel Phantom. *J Med Ultrasound*. 2021;29(4):239-249. doi:10.4103/JMU.JMU

44. Drakos T, Giannakou M, Menikou G, Ioannides C, Damianou C. An improved method to estimate ultrasonic absorption in agar-based gel phantom using thermocouples and MR thermometry. *Ultrasonics*. 2020;103. doi:10.1016/j.ultras.2020.106089

45. Menikou G, Yiannakou M, Yiallouras C, Ioannides C, Damianou C. MRI-compatible bone phantom for evaluating ultrasonic thermal exposures. *Ultrasonics*. 2016;71:12-19. doi:10.1016/j.ultras.2016.05.020

46. Antoniou A, Damianou C. MR relaxation properties of tissue-mimicking phantoms. *Ultrasonics*. 2022;119. doi:10.1016/j.ultras.2021.106600

47. Drakos T, Giannakou M, Menikou G, Constantinides G, Damianou C. Characterization of a soft tissue-mimicking agar/wood powder material for MRgFUS applications. *Ultrasonics*. 2021;113: 10635. doi:10.1016/j.ultras.2021.106357

48. Liberman G, Louzoun Y, Ben Bashat D. T1 Mapping using variable flip angle SPGR data with flip angle correction. *J Magn Reson Imaging*. 2014;40(1):171-180. doi:10.1002/jmri.24373

49. Bojorquez JZ, Bricq S, Acquitter C, Brunotte F, Walker PM, Lalande A. What are normal relaxation times of tissues at 3 T? *Magn Reson Imaging*. 2017;35(2017):69-80. doi:10.1016/j.mri.2016.08.021

50. Giannakou M, Yiallouras C, Menikou G, Ioannides C, Damianou C. MRI-guided frameless biopsy robotic system with the inclusion of unfocused ultrasound transducer for brain cancer ablation. *Int J Med Robot Comput Assist Surg*. 2019;15(1):1-9. doi:10.1002/rcs.1951

51. Epaminonda E, Drakos T, Kalogirou C, Theodoulou M, Yiallouras C, Damianou C. MRI guided focused ultrasound robotic system for the treatment of gynaecological tumors. *Int J Med Robot Comput Assist Surg*. 2016;12:46-52. doi:10.1002/rcs.1653

52. Yiallouras C, Damianou C. Review of MRI positioning devices for guiding focused ultrasound systems. *Int J Med Robot Comput Assist Surg*. 2015;11:247-255. doi:10.1002/rcs.1601.

53. Yiannakou M, Menikou G, Yiallouras C, Ioannides C, Damianou C. MRI guided

focused ultrasound robotic system for animal experiments. *Int J Med Robot Comput Assist Surg*. 2017;13(4):e1804. doi:10.1002/rcs.1804

54. Menikou G, Yiallouras C, Yiannakou M, Damianou C. MRI-guided focused ultrasound robotic system for the treatment of bone cancer. *Int J Med Robot Comput Assist Surg*. 2017;13(1):1-11. doi:10.1002/rcs.1753

55. Antoniou A, Giannakou M, Evripidou N, Stratis S, Pichardo S, Damianou C. Robotic system for top to bottom MRgFUS therapy of multiple cancer types. *Int J Med Robot Comput Assist Surg*. 2022. doi:10.1002/rcs.2364

56. Antoniou A, Giannakou M, Georgiou E, Kleopa KA, Damianou C. Robotic device for transcranial focussed ultrasound applications in small animal models. *Int J Med Robot Comput Assist Surg*. 2022:1-11. doi:10.1002/rcs.2447

57. Phantom-based assessment of accuracy of motion and needle targeting of robotic devices for MRI-guided breast biopsy.

58. Drakos T, Giannakou M, Menikou G, et al. MRI-Guided Focused Ultrasound Robotic System for Preclinical use. *J Vet Med Anim Sci*. 2021;4(1):1-11.

59. Drakos T, Giannakou M, Menikou G, Damianou C. Magnetic Resonance Imaging–Guided Focused Ultrasound Positioning System for Preclinical Studies in Small Animals. *J Ultrasound Med*. 2020:1-10. doi:10.1002/jum.15514

60. Giannakou M, Antoniou A, Damianou C. Preclinical robotic device for MRI guided focused ultrasound. *Int J Med Robot Comput Assist Surg*. 2022;(e2466):1-10. doi:10.1002/rcs.2466

61. Stoianovici D, Kim C, Srimathveeravalli G, Sebrecht P. MRI-safe Robot for Endorectal

Prostate Biopsy. *IEEE ASME Trans Mechatron*. 2014;19(4):1289-1299. doi:10.1109/TMECH.2013.2279775.MRI-Safe

62. Antoniou A, Georgiou L, Christodoulou T, et al. MR relaxation times of agar-based tissue-mimicking phantoms. *J Appl Clin Med Phys*. 2022:213533. doi:10.1002/acm2.13533

63. Bottomley PA, Foster TH, Argersinger RE, Pfeifer LM. A review of normal tissue hydrogen NMR relaxation times and relaxation mechanisms from 1–100 MHz: Dependence on tissue type, NMR frequency, temperature, species, excision, and age. *Int J Med Phys Res Pract*. 1984;11(4):425-448. doi:10.1118/1.595535

64. Stanisz GJ, Odrobina EE, Pun J, et al. T1, T2 relaxation and magnetization transfer in tissue at 3T. *Magn Reson Med*. 2005;54(3):507-512. doi:10.1002/mrm.20605

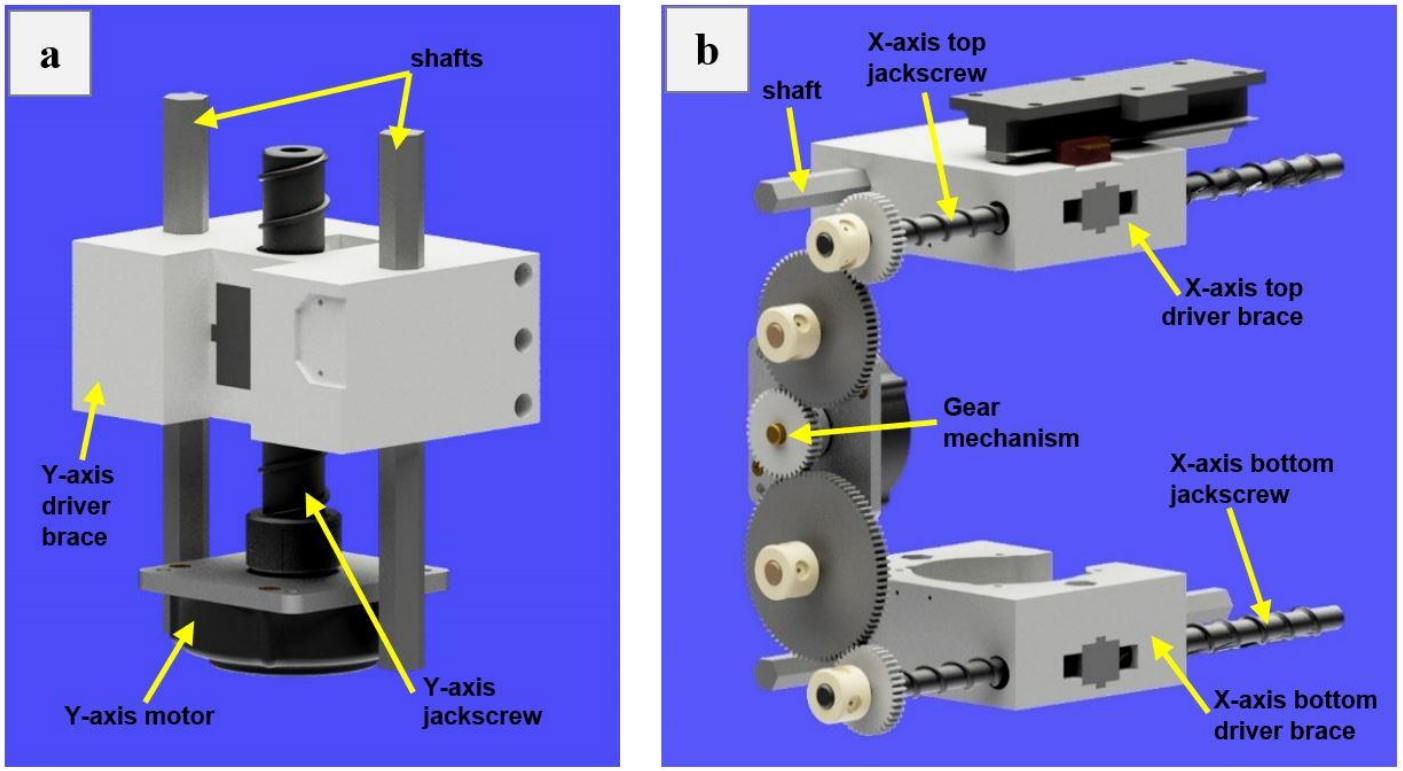
a
shafts
Y-axis
driver
brace
Y-axis motor
Y-axis
jackscrew
b
shaft
X-axis top
jackscrew
X-axis top
driver brace
Gear
mechanism
X-axis bottom
jackscrew
X-axis bottom
driver brace

Figure 1

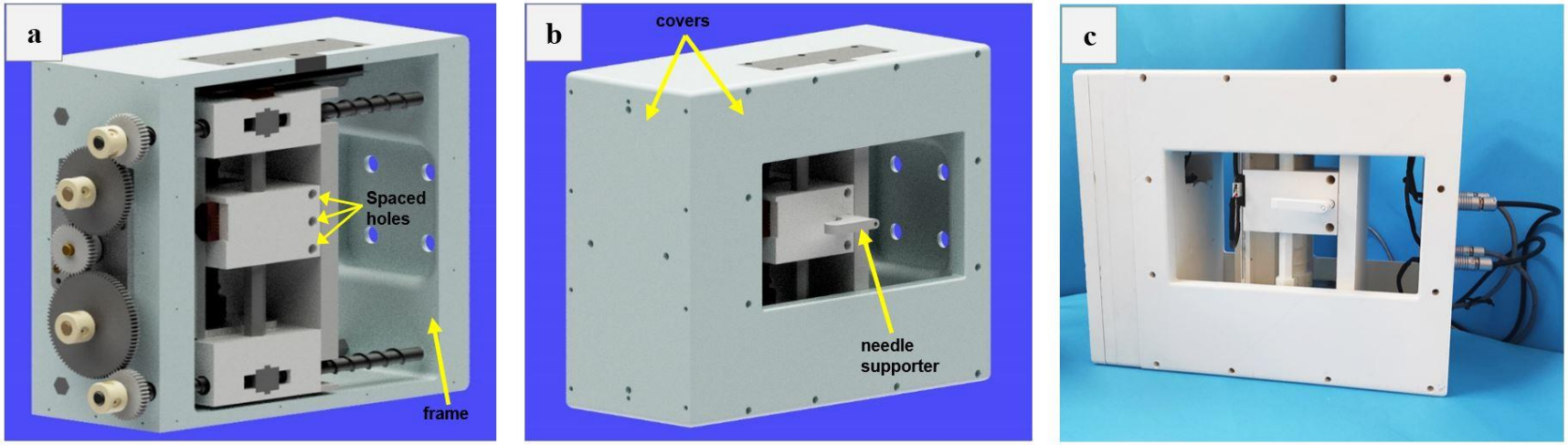

Figure 2

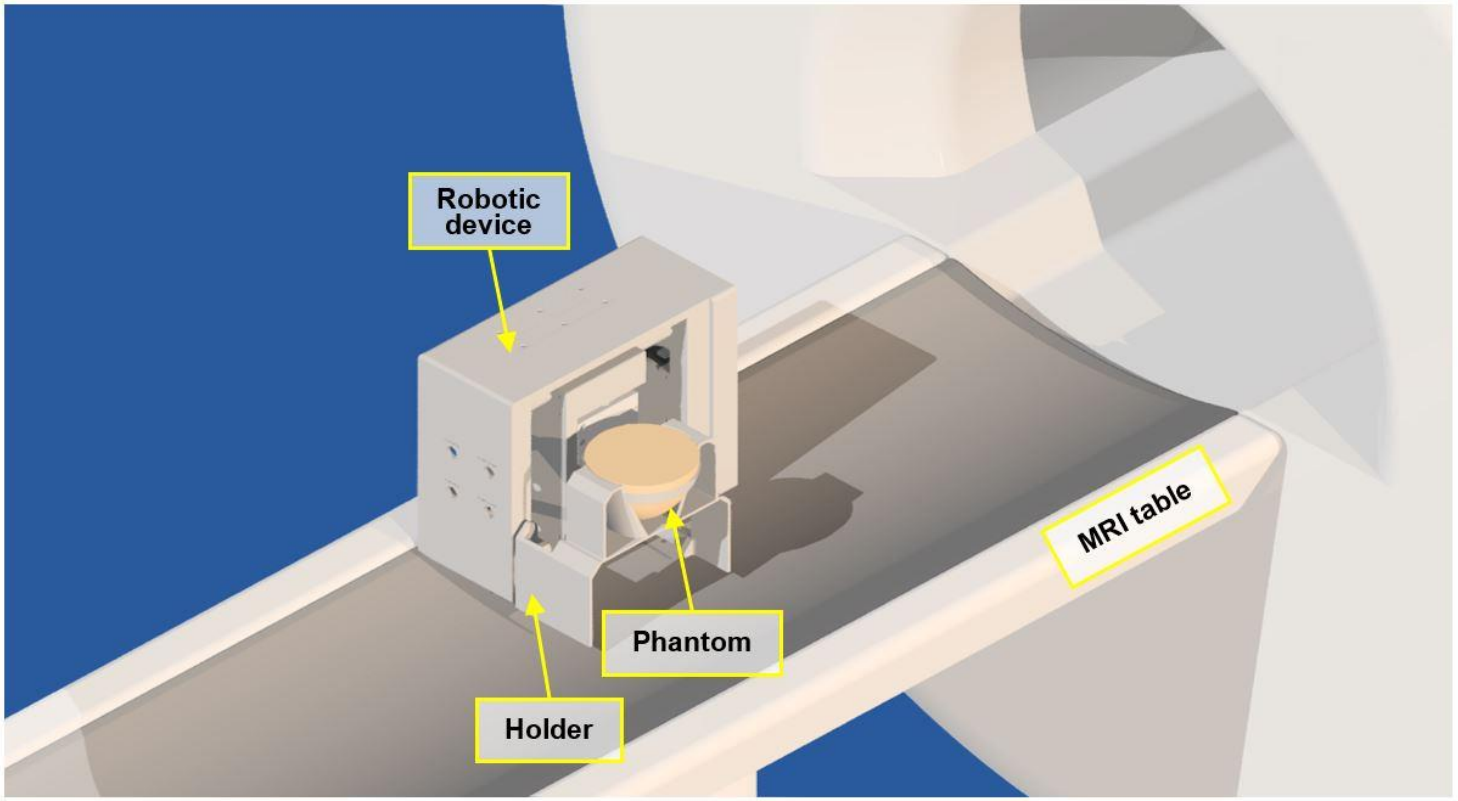

Figure 3

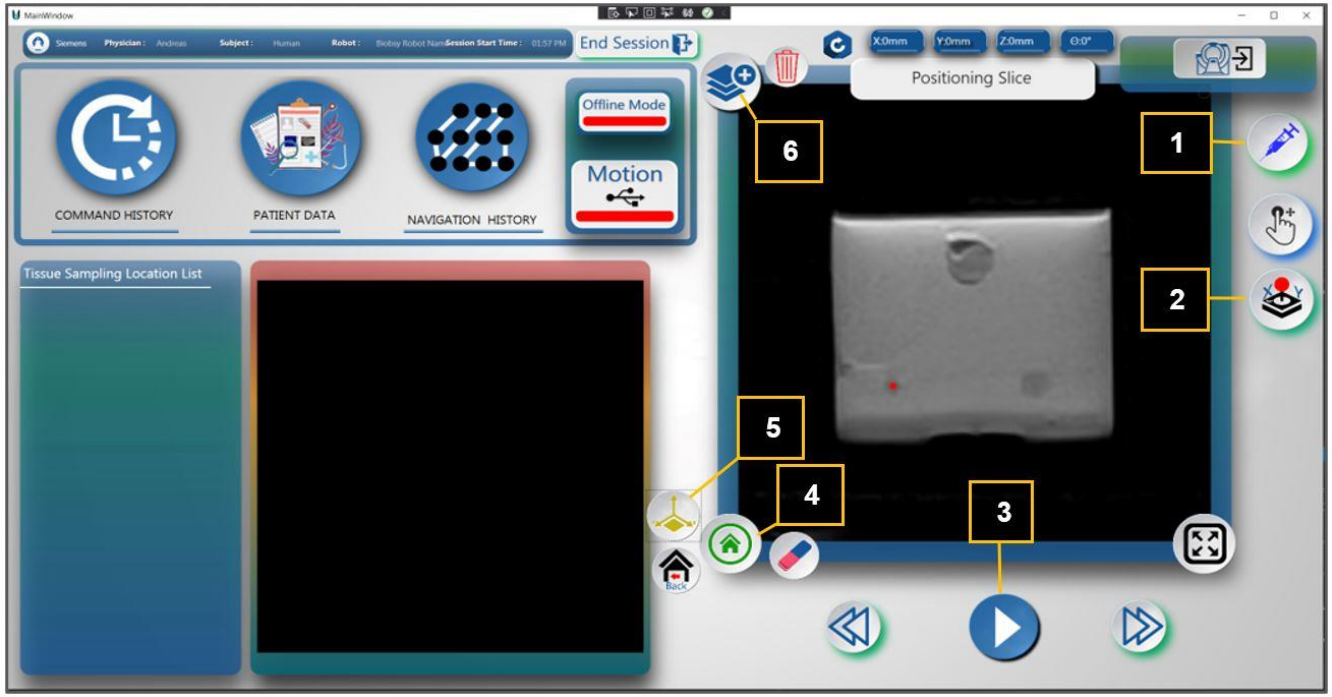
End Session
Offline Mode
Motion
COMMAND HISTORY
PATIENT DATA
NAVIGATION HISTORY
Tissue Sampling Location List
Positioning Slice
X:0mm
Y:0mm
Z:0mm
1
2
3
4
5
6

Figure 4

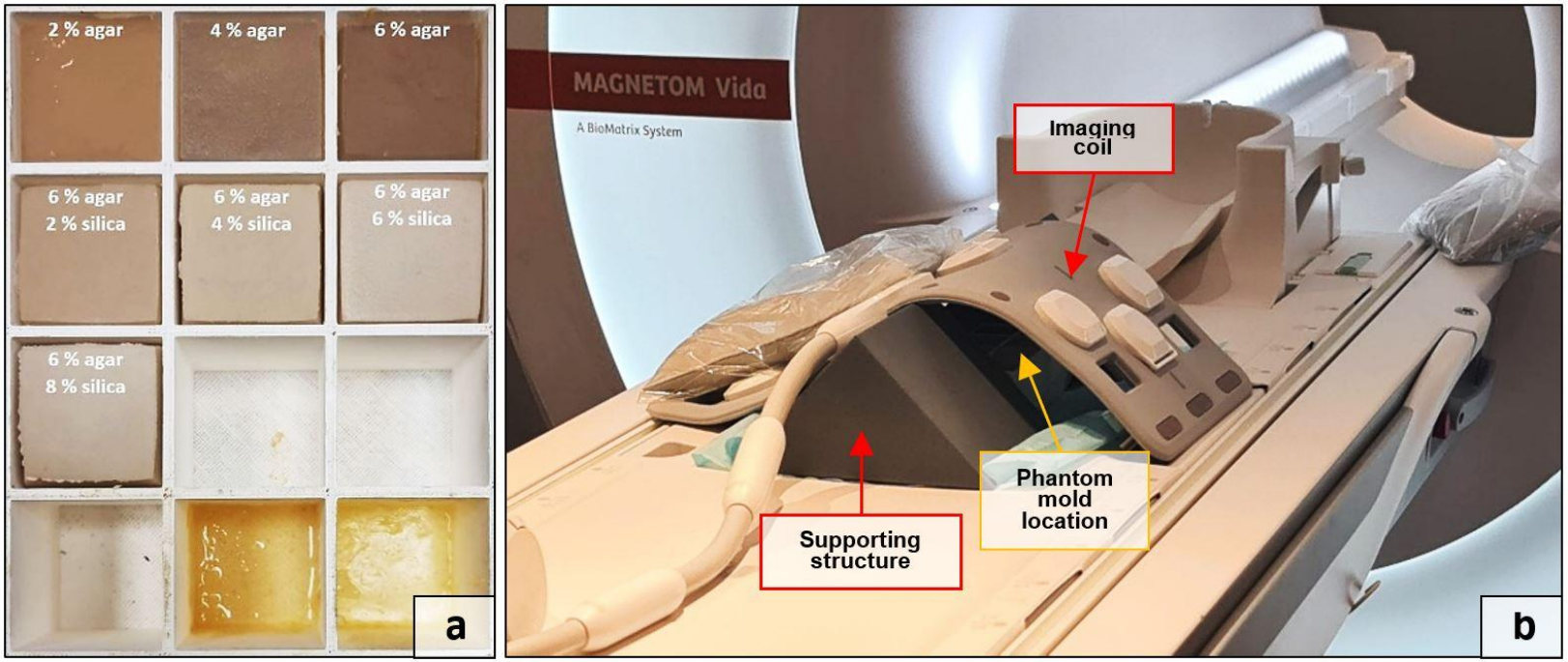
2 % agar
4 % agar
6 % agar
6 % agar
2 % silica
6 % agar
4 % silica
6 % agar
6 % silica
6 % agar
8 % silica
a
MAGNETOM Vida
A BioMatrix System
Imaging coil
Phantom mold location
Supporting structure
b

Figure 5

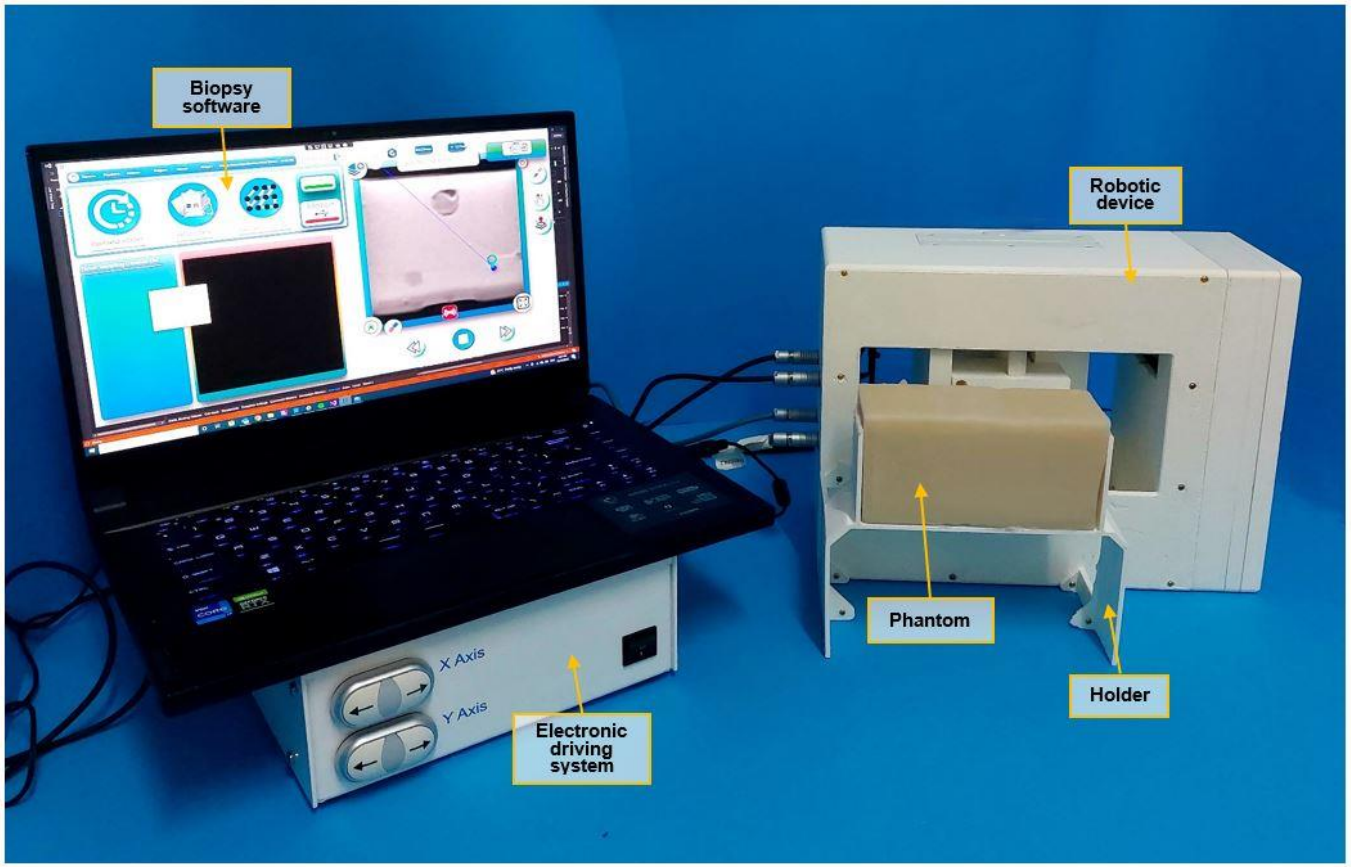
Biopsy software
Robotic device
Phantom
Holder
X Axis
Y Axis
Electronic driving system

Figure 6

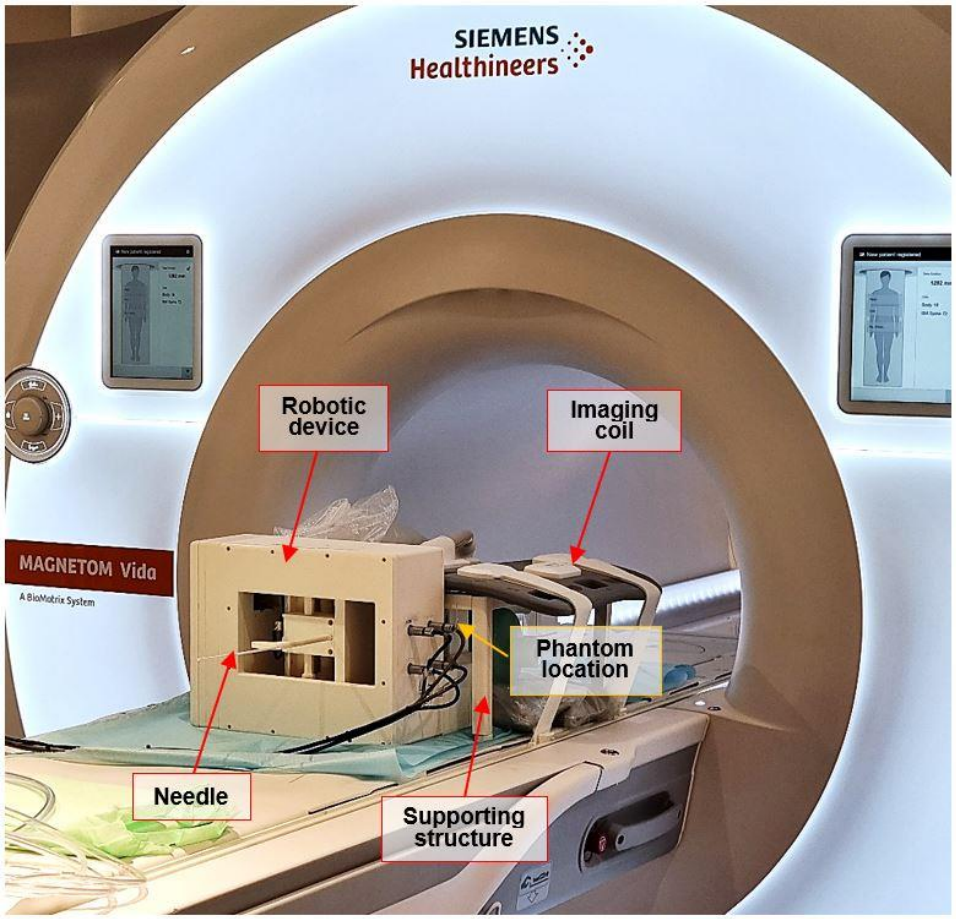
SIEMENS
Healthineers
Robotic device
Imaging coil
MAGNETOM Vida
A BioMatrix System
Phantom location
Needle
Supporting structure

Figure 7

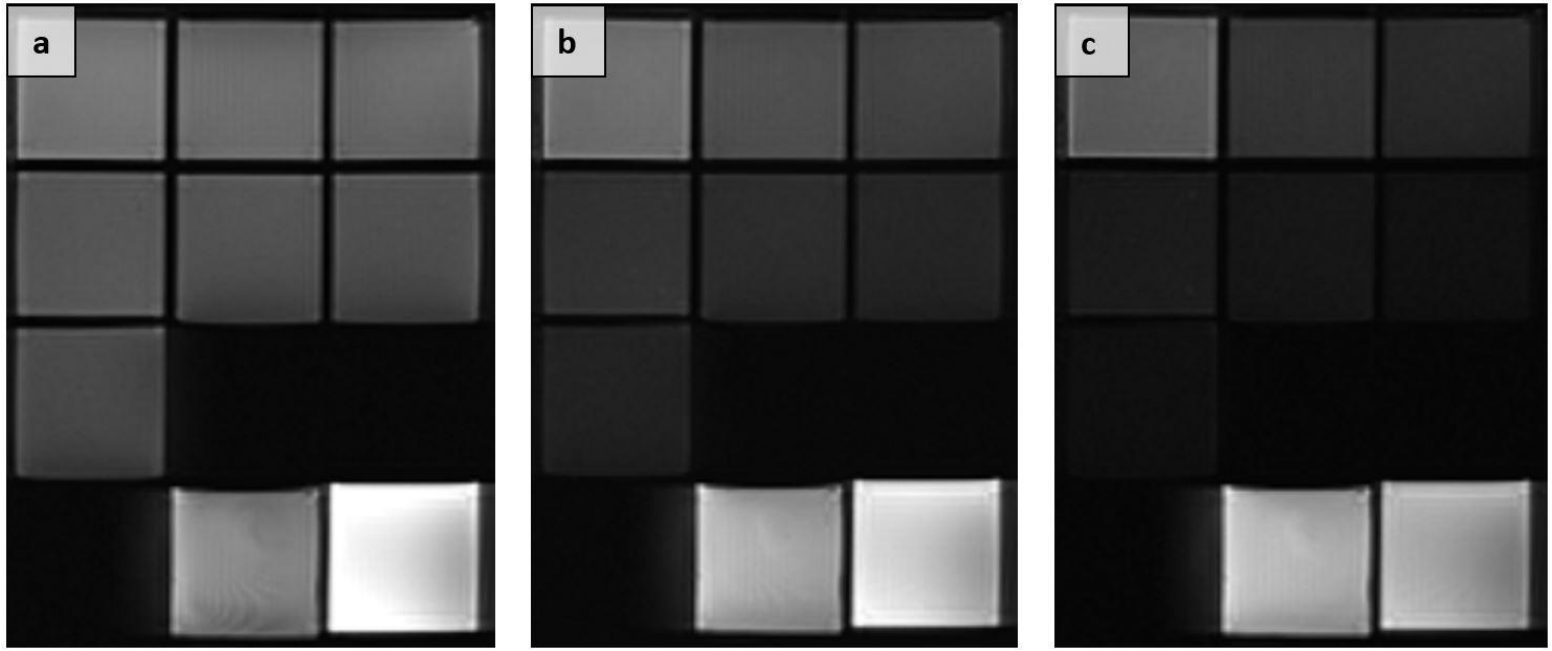

Figure 8

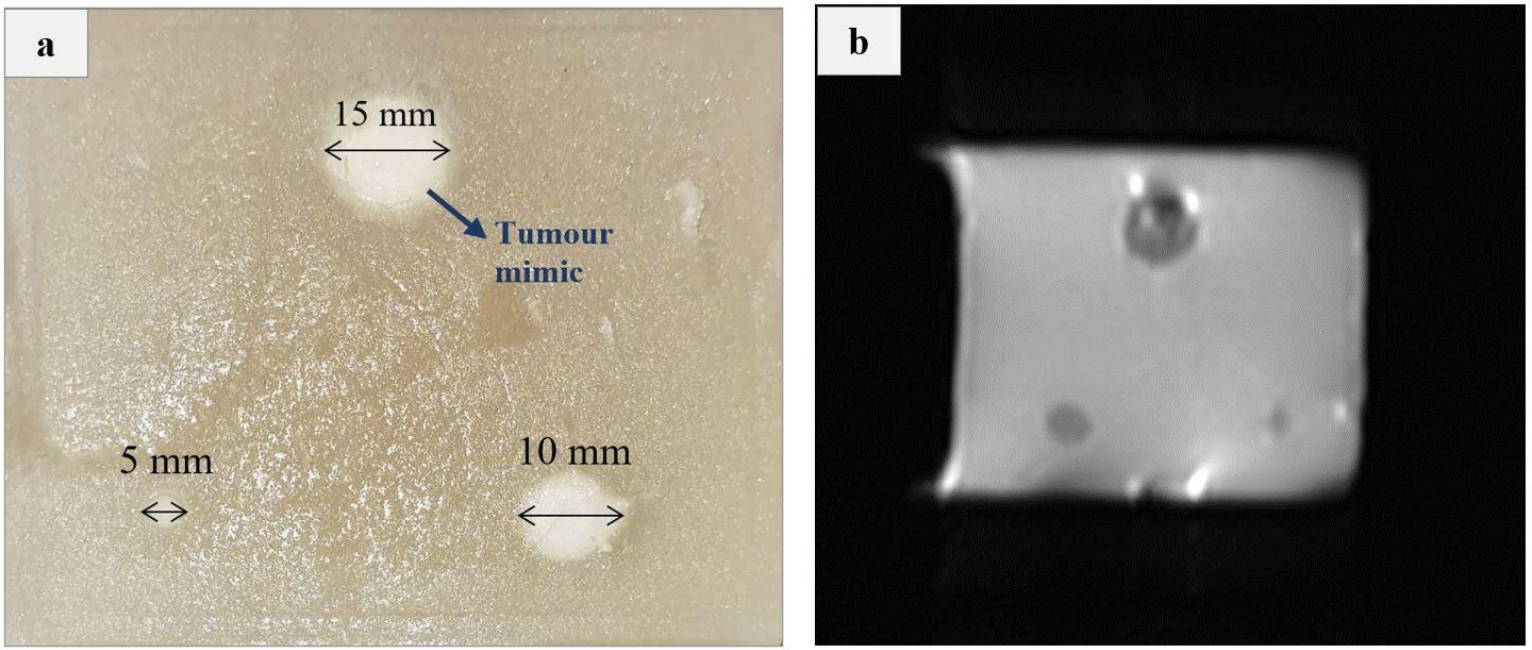

Figure 9

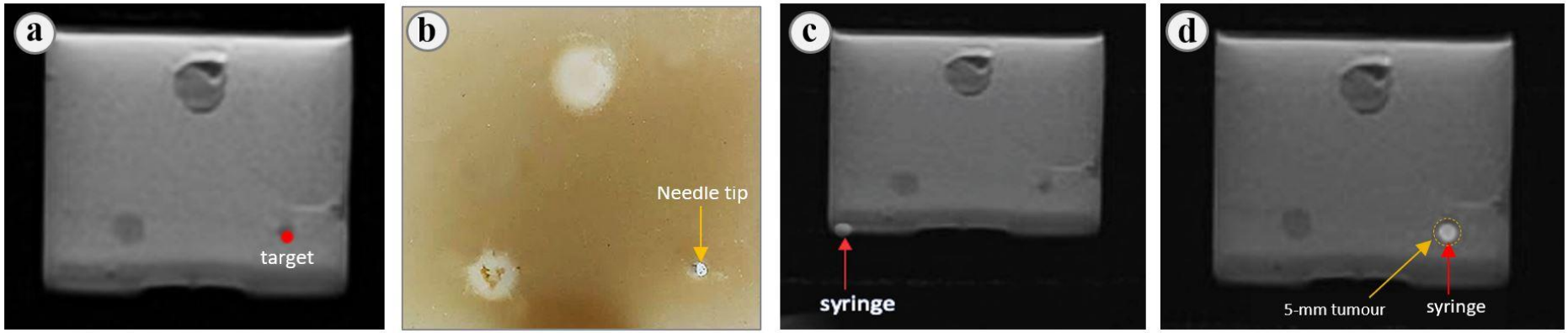

Figure 10

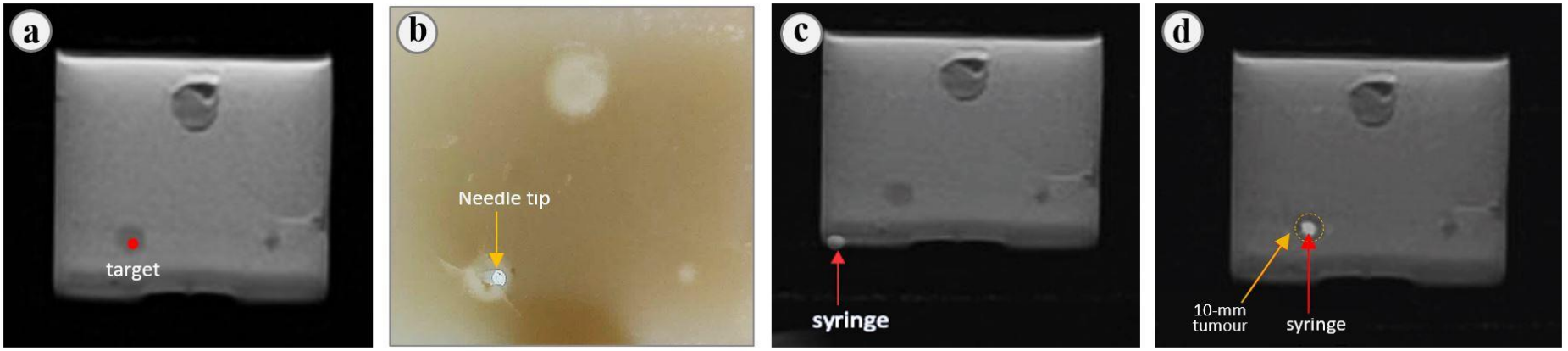

Figure 11